

## **ABSTRACT**

**CAULFIELD, FRANCIS DONALD.** Electromechanical Actuator Development for Integrated Chatter Prediction on High Speed Machining Centers. (Under the direction of Gregory Dale Buckner)

Machine tool chatter imposes limitations on the productivity and quality of modern high speed machining (HSM) operations. It has been shown that chatter prediction and avoidance strategies can lead to increased machining productivity if certain modal characteristics of the machine are known. The objectives of this research are to design and demonstrate an electromechanical actuator (EMA) to easily and accurately identify these characteristics. Design specifications for this actuator reflect a wide range of machine tools and operating conditions. A simulation-based design strategy is employed, based on traditional electromechanical analysis, finite element analysis (FEA), and computer simulations to ensure performance meets the design specifications. A prototype EMA system is built to validate the analytical results and demonstrate its capabilities as part of an automated chatter prediction and avoidance system. The EMA is shown to generate the required modal characteristics, namely frequency response functions (FRFs) and stability lobe diagrams (SLDs) quickly, accurately, and with fewer technical skill requirements than other vibration testing methods. Experimental machining tests demonstrate that the EMA can be an effective component of an integrated chatter prediction and avoidance system.

**ELECTROMECHANICAL ACTUATOR DEVELOPMENT FOR  
INTEGRATED CHATTER PREDICTION ON  
HIGH SPEED MACHINING CENTERS**

by

**FRANCIS DONALD CAULFIELD**

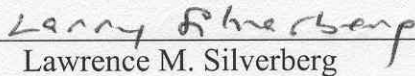
A thesis submitted to the Graduate Faculty of  
North Carolina State University  
in partial fulfillment of the  
requirements for the Degree of  
Master of Science

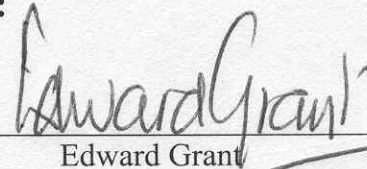
**MECHANICAL ENGINEERING**

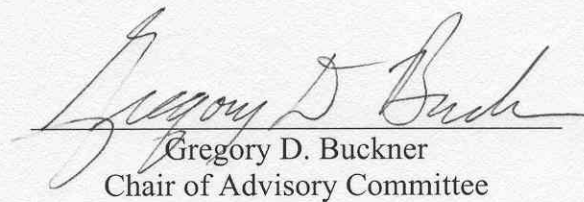
Raleigh

2002

**APPROVED BY:**

  
Lawrence M. Silverberg

  
Edward Grant

  
Gregory D. Buckner  
Chair of Advisory Committee

## **Biography**

Don Caulfield was born in Mendham, New Jersey and found his way to Raleigh, North Carolina where he graduated Magna Cum Laude from North Carolina State University with a Bachelor of Science in Mechanical Engineering in 2000. He followed this with a Master of Science in Mechanical Engineering at the same university, graduating Magna Cum Laude in 2002.

## **Acknowledgments**

I would like to thank Dr. Donald Esterling of VulcanCraft, Inc. for his generous support of this research. I would also like to thank my advisor, Dr. Gregory Buckner, for his support, enthusiasm, and guidance throughout the process. I am also grateful for the assistance and encouragement of Dr. Larry Silverberg and Dr. Eddie Grant, members of my graduate committee.

Finally, I wish to thank my family for their unending support, especially my wife Regina who made me do it.

# Table of Contents

<b>List of Tables .....</b>	<b>vi</b>
<b>List of Figures .....</b>	<b>vii</b>
<b>List of Symbols .....</b>	<b>ix</b>
<b>1 Introduction .....</b>	<b>1</b>
<b>2 High Speed Machining .....</b>	<b>4</b>
2.1 Background.....	4
2.2 HSM.....	4
2.3 Chatter.....	6
2.3.1 Regenerative Chatter.....	7
2.3.2 Stability Lobe Diagrams (SLDs) .....	9
2.4 Predicting, Identifying and Controlling Chatter .....	11
2.4.1 Traditional Methods of Chatter Avoidance.....	11
2.4.2 Modern Efforts to Overcome the Problem.....	12
2.4.3 In-situ Chatter Control .....	12
2.4.4 A Priori Chatter Prediction .....	13
2.5 The NIST PM Testing Implementation.....	16
2.6 Electromechanical Actuation.....	17
<b>3 Modal Testing .....</b>	<b>18</b>
3.1 Overview.....	18
3.2 Impact Hammer Testing .....	19
3.3 Shaker Testing .....	20
3.4 Non-contacting EMA Testing .....	21
3.4.1 Benefits of Non-contacting Actuation .....	21
<b>4 Design of the Electromechanical Actuator .....</b>	<b>24</b>
4.1 Design Overview .....	24
4.2 Design Specifications .....	27
4.3 Analytical Design and Simulation .....	30
4.3.1 EMA Modeling Overview .....	31
4.3.2 Magnetic Circuit Analysis .....	32
4.3.3 Electrical Dynamics.....	36
4.3.4 Generalized Machine Theory.....	38
4.3.5 Electromechanical Dynamics.....	40
4.4 Design Parameters .....	42

4.5 <i>Finite Element Analysis and Simulation</i> .....	44
4.5.1 FEMM <sup>®</sup> .....	44
4.5.2 Analysis Setup .....	45
4.5.3 FEA Results, Comparison With MCA and GMT Results .....	47
4.6 <i>Design Summary</i> .....	49
<b>5 EMA System Hardware</b> .....	<b>50</b>
5.1 <i>EMA Design Overview</i> .....	50
5.2 <i>EMA Core</i> .....	51
5.3 <i>EMA Coil</i> .....	52
5.4 <i>EMA Mounting System</i> .....	53
5.5 <i>Optical Displacement Sensor and Mounting Post</i> .....	57
5.6 <i>EMA Housing</i> .....	60
5.7 <i>Real-time Control Chassis</i> .....	60
<b>6 Experimental Evaluations</b> .....	<b>63</b>
6.1 <i>Test Objectives</i> .....	63
6.2 <i>Verification of EMA Flux Characteristics</i> .....	63
6.3 <i>Verification of EMA Force Characteristics</i> .....	64
6.4 <i>EMA Modal Tests</i> .....	66
6.4.1 <i>EMA Modal Tests: Non-Rotating Tools</i> .....	66
6.4.2 <i>EMA Modal Tests: Rotating Tools</i> .....	72
6.5 <i>Stability Lobe Diagram Verification</i> .....	75
6.6 <i>Summary of Test Results</i> .....	81
<b>7 Conclusions and Future Work</b> .....	<b>82</b>
7.1 <i>Conclusions</i> .....	82
7.2 <i>Future Work</i> .....	83
7.2.1 <i>Real-time Data Filtering</i> .....	83
7.2.2 <i>Self-Sensing Capabilities</i> .....	84
<b>References</b> .....	<b>85</b>

## List of Tables

Table 4.1: EMA design requirements .....	30
Table 4.2: Electrical circuit components and electromagnetic equivalents .....	32
Table 4.3: Critical assumptions of magnetic circuit analysis .....	33
Table 4.4: EMA-specific design assumptions .....	34
Table 4.5: EMA sample force calculation data.....	43
Table 4.6: EMA force calculation data.....	44
Table 4.7: FEMM <sup>®</sup> triangular mesh element edge sizes .....	46
Table 5.1: Philtec RC25 output specifications.....	58
Table 6.1: EMA modal testing summary for non-rotating specimens.....	68
Table 6.2: EMA modal testing summary for rotating specimens.....	73
Table 6.3: Computed RMS accelerations for 0.7 mm deep slotting cuts .....	79

## List of Figures

Figure 2.1: F-15 speed brake produced by Boeing, St. Louis, MO .....	5
Figure 2.2: In-phase cut [39].....	7
Figure 2.3: Out-of-phase cut [39] .....	8
Figure 2.4: Rough surface finish caused by tool chatter.....	9
Figure 2.5: Stability lobe diagram [39].....	10
Figure 2.6: Ingersoll's chatter detection flowchart for existing systems (cutting and not cutting) [26] .....	14
Figure 2.7: NIST PM passive machine tool actuator [30] .....	16
Figure 3.1: Impact hammer testing for modal analysis [16].....	19
Figure 3.2: EMA system in test configuration.....	23
Figure 4.1: Profile of the electromechanical actuator.....	25
Figure 4.2: Iron-core relay with return spring .....	31
Figure 4.3: EMA pole configuration.....	32
Figure 4.4: Equivalent magnetic circuit of EMA.....	34
Figure 4.5: Electromechanical energy conversion element.....	38
Figure 4.6: FEMM <sup>®</sup> actuator geometry .....	45
Figure 4.7: Actuator geometry analyzed with FEMM <sup>®</sup> .....	46
Figure 4.8: Flux analysis results of the EMA .....	47
Figure 4.9: Magnetic flux in the air gaps.....	48
Figure 4.10: EMA force predictions: FEMM <sup>®</sup> and GMT .....	49
Figure 5.1: Actuator hardware with on-board optical displacement sensor .....	50
Figure 5.2: EMA core geometry .....	51
Figure 5.3: EMA core laminations.....	52
Figure 5.4: EMA coil .....	53
Figure 5.5: EMA mounting system.....	54
Figure 5.6: EMA mounting baseplate (all dimensions inches).....	54
Figure 5.7: EMA spider mounting plate (all dimensions in inches).....	55
Figure 5.8: EMA baseplate clamped in workpiece vise for testing .....	56

Figure 5.9: PCB 201M73 calibration curve.....	57
Figure 5.10: Philtec RC25 calibration curve.....	58
Figure 5.11: ODS support and adjustment insert post.....	59
Figure 5.12: ODS a) base and b) adjustment sensor post (all dimensions inches).....	59
Figure 5.13: EMA housing (all dimensions inches).....	60
Figure 5.14: Simulink <sup>®</sup> real-time data acquisition and control program.....	61
Figure 5.15: Real-time control chassis interior.....	62
Figure 6.1: Experimental measurements and FEA predictions of EMA flux density vs. applied magnetic field.....	64
Figure 6.2: Experimental measurements and FEA predictions of EMA force amplitude	65
Figure 6.3: Closeup of actuator in test position.....	67
Figure 6.4: EMA and impact hammer (10 averages) FRFs for a 4.00” overhang tool blank .....	69
Figure 6.5: EMA and impact hammer (10 averages) FRFs for a 6.00” overhang tool blank .....	70
Figure 6.6: EMA and impact hammer (10 averages) FRFs for a 3.50” overhang, 4-flute HSS end mill.....	71
Figure 6.7: Closeup of half-round tool blank.....	72
Figure 6.8: EMA force profile used to excite rotating half-round tool blanks a) low frequency sinusoidal pulse b) higher frequency sinusoidal pulse.....	73
Figure 6.9: EMA FRF of a 3.50” overhang, half-round tool blank rotating at 1200 rpm	74
Figure 6.10: SLD for a 4.00”, 4-flute HSS end mill [28].....	76
Figure 6.11: Acceleration time responses for a 4.00” overhang, 4-flute end mill at three different spindle speeds: 0.7 mm cutting depth.....	78
Figure 6.12: Acceleration frequency responses for a 4.00” overhang, 4-flute end mill at three different spindle speeds: 0.7 mm cutting depth.....	79
Figure 6.13: Cutting test results for 4.00” overhang, 4-flute end mill [28].....	80

## List of Symbols

$A$	= cross-sectional area of flux path ( $\text{m}^2$ )
$A_c$	= cross-sectional area of flux path through actuator core ( $\text{m}^2$ )
$A_g$	= cross-sectional area of flux path through actuator air gap ( $\text{m}^2$ )
$A_r$	= cross-sectional area of coil wire ( $\text{m}^2$ )
$A_t$	= cross-sectional area of flux path through cutting tool ( $\text{m}^2$ )
$b$	= stability lobe boundary (mm)
$b_{lim}$	= limit of stability (mm)
$b_s$	= system damping parameter ( $\text{N}\cdot\text{s}/\text{m}$ )
$B$	= flux density (T)
$\hat{B}$	= maximum flux density (T)
$c$	= lamination thickness (m)
$d$	= diameter of circular beam/cutting tool (m)
$E$	= Young's modulus (GPa)
$f_f$	= flute passing frequency (Hz)
$f_n$	= system first natural frequency (Hz)
$\mathcal{F}(t)$	= magnetomotive force, $mmf$ (A-turns)
$F_a(t)$	= actuator force (N)
$F_d(t)$	= internal damping force of tool (N)
$F_{em}(t)$	= controllable reluctance force (N)
$F_k(t)$	= spring force of deflected cutting tool (N)
$F_{min}$	= minimum actuator force (N)
$i(t)$	= current in the EMA coils (A)
$I$	= area moment of inertia ( $\text{m}^4$ )
$j$	= integer representing stable cuts
$k$	= stiffness constant ( $\text{N}/\text{m}$ )
$K_s$	= specific force of the workpiece material ( $\text{N}/\text{mm}^2$ )
$l$	= length of a beam (m)
$l_c$	= length of flux path through actuator core (m)

- $l_g(t)$  = length of flux path through actuator air gap (m)  
 $l_{gnom}$  = nominal length of flux path through actuator air gap (m)  
 $l_i$  = mean length of the magnetic flux path through the  $i^{\text{th}}$  component (m)  
 $l_r$  = coil wire length (m)  
 $l_t$  = length of flux path through cutting tool (m)  
 $L$  = actuator winding inductance (H)  
 $m$  = mass (kg)  
 $m_l$  = mass/unit length of a beam (kg/m)  
 $m_t$  = mass of tool (kg)  
 $n$  = spindle speed (rev/min)  
 $n_c$  = number of coils in winding  
 $N$  = number of flutes on milling tool  
 $\bar{p}$  = average power loss per unit conductor volume (W)  
 $R$  = resistance ( $\Omega$ )  
 $\mathcal{R}_c$  = electromagnetic reluctance of actuator core material (Amp-turns/Weber)  
 $\mathcal{R}_{eq}$  = equivalent electromagnetic reluctance (Amp-turns/Weber)  
 $\mathcal{R}_{g1}$  = electromagnetic reluctance of air gap 1 (Amp-turns/Weber)  
 $\mathcal{R}_{g2}$  = electromagnetic reluctance of air gap 2 (Amp-turns/Weber)  
 $\mathcal{R}_t$  = electromagnetic reluctance of cutting tool (Amp-turns/Weber)  
 $Re(G)$  = real part of the tool/spindle/machine system FRF  
 $V_i(t)$  = voltage induced by change in flux linkage (V)  
 $V_R(t)$  = resistive voltage (V)  
 $V_s(t)$  = applied coil voltage (V)  
 $x(t)$  = cutting tool displacement (m)  
 $\Delta l_g(t)$  = change in length of flux path through actuator air gap (m)  
 $\theta$  = actuator core pole cutaway angle (degrees)  
 $\lambda(t)$  = flux linkage (Amp-turns)  
 $\mu$  = relative permeability of magnetic circuit component (H/m)

- $\mu_c$  = relative permeability of actuator core (H/m)
- $\mu_d$  = directional orientation factor
- $\mu_g$  = relative permeability of air gap (H/m)
- $\mu_t$  = relative permeability of cutting tool (H/m)
- $\rho$  = resistivity of coil wire ( $\Omega \cdot m$ )
- $\Phi(t)$  = magnetic flux (Webers)
- $\omega$  = signal (current) frequency (rad/sec)

# 1 Introduction

Recent advancements in the design of machining centers have increased commercially available spindle speeds to over 40,000 rpm. Enhanced machine capabilities have given rise to the practical implementation of high speed machining (HSM). While HSM is difficult to define precisely, it generally involves running machines at higher spindle speeds and higher feed rates, thereby increasing production rates in manufacturing shops. HSM is gaining widespread acceptance in manufacturing sectors, with its adoption being led by the aerospace industry. Large aluminum parts can be produced from a single workpiece using HSM methods, instead of requiring assembly from many components. Besides the time saved in assembly, other benefits include reduced lead time, reduced waste, and parts that are simultaneously lighter, stronger, and cheaper. The tool and die industry is also rapidly adopting HSM [24]. The use of HSM will become more widespread in industry as its benefits become better understood.

There are problems associated with the increased spindle speeds of HSM, most notably tool chatter. Chatter is an unstable vibration of the cutting tool [5] that is a function of both spindle speed and cutting depth. It can cause problems ranging from poor surface finish to machine damage and personal injury. The intuitive method of chatter avoidance dictates that whenever chatter is encountered the spindle speed should be reduced. This eliminates the production gains made possible by purchasing and using a high-speed machine.

Several methods have been devised to control, prevent, or avoid chatter. These methods range from sampling acoustic signals while cutting is in progress [17] to predicting machine behavior by a priori characterization of the system dynamics [1, 7]. Chatter control methods that use real-time measurements can be effective in controlling chatter after its onset, but these techniques have the disadvantage of not being able to prevent chatter from occurring.

Predictive methods offer the benefit of avoiding the onset of chatter in the first place. Sophisticated techniques such as finite element analysis (FEA) can be used to characterize the machine's dynamics. FEA can accurately predict the frequency response characteristics of the system [7], but requires experimental verification and the input of experimentally derived parameters. It is also time consuming and computationally intensive. Experimental modal testing provides the essential information of FEA, namely the system's frequency response functions (FRFs), and is quicker to perform. Unfortunately, modal testing requires specialized equipment and skills that make it impractical for widespread industrial adoption.

Researchers at NIST have devised an automated technique that can produce frequency response information quickly without requiring special skills [5]. This method uses a stationary permanent magnet to impart excitation forces to a rotating tool. Tool displacement is measured using optical sensors, and frequency response information is calculated using data acquisition and analysis software. This approach shows potential for automated chatter prediction. The components of the system (a permanent magnet, off-the-shelf sensors and data acquisition hardware and software) suggest that a system using this method would be inexpensive to produce. However, the inability to control the applied force magnitudes using a permanent magnet restricts the feasibility of this approach.

A refined approach is developed in this research to measure the frequency response characteristics of a high-speed milling machine and predict stable operating regions. This approach offers the benefits of the NIST scheme (ease of use, minimal testing time, low expenses of production), but overcomes the limitations of passive excitation by introducing a controlled, non-contacting electromechanical actuator. This high-bandwidth actuator delivers accurately shaped, high-magnitude excitation forces to the tool (rotating or stationary) and enables accurate prediction of the frequency response characteristics. The research outlined in this thesis relies on theory, simulation, and

experimental validations. A prototype actuator is designed, fabricated, and experimentally validated on a CNC machining center.

Preliminary results show that the electromechanical actuator has sufficient bandwidth, force magnitude, and pulse-shaping capabilities to be an effective component in an automated chatter prediction system. The actuator is successfully demonstrated using a variety of tool materials and geometries. Frequency response functions produced with the actuator closely match those produced with impact hammer tests. Most importantly, regions of stable (chatter-free) machining are predicted and experimentally validated using this approach.

## **2 High Speed Machining**

### **2.1 Background**

Maximizing productivity is a primary goal in the machine shop environment. For milling processes, this frequently translates into maximizing the material removal rate (MRR). Possible mechanisms for increasing the MRR include 1) increasing the spindle speed, 2) increasing the cutting depth, and 3) increasing the feed rate. There are practical limits on the spindle speeds and feed rates at which a milling machine can be operated. Similarly, material considerations in the tool and machine impose limits on the cutting depth.

Advances in milling machine technology have enabled manufacturers to produce machines with spindle speeds exceeding 40,000 rpm. These high spindle speeds enable very high MRRs through a process known as high speed machining (HSM). Although the definition of HSM is inexact, it is usually related to spindle speed. A useful definition offered by Dr. Scott Smith at the University of North Carolina at Charlotte suggests that HSM is “machining at or near the resonant frequencies of the tool or machine” [24].

Seventy-five years of HSM research has resulted in the identification of stable cutting regions for high-speed spindles [1, 38]. While HSM promises great productivity gains, there are drawbacks and limitations associated with this technology that are impeding its widespread adoption in smaller machining facilities. The following section discusses the implications of HSM as well as problems associated with the increased spindle speeds.

### **2.2 HSM**

HSM is currently finding application mainly in the aerospace industry, although a recent white paper from Unigraphics, Inc. suggests that “approximately 30 percent of the companies in the U.S. and Japan are already using HSM, with the number even greater in Germany at 40 percent. The remaining companies in all these countries are considering making an investment in HSM or are interested in this new technology” [41]. HSM will

find its way into smaller machine shops as it becomes better understood and its drawbacks are addressed.

The main advantage of HSM is that it gives manufacturers a practical and cost-effective way to produce parts that cannot be as easily produced using standard machining processes. Examples of this benefit can be found in aircraft parts produced by Boeing at their Advanced Materials Fabrication Facility in St. Louis, MO. These parts are simultaneously lighter, stronger, cheaper, and require a small fraction of the machine time previously needed [24]. One of the parts Boeing produces using HSM is the F-15 fighter's speed brake (Figure 2.1). This part was previously assembled from 500 individual components, but HSM enables Boeing to mill this part out of a single block of aluminum. The manufacturing lead time for this part has reduced from three months to only a few days.



**Figure 2.1: F-15 speed brake produced by Boeing, St. Louis, MO**

The absence of stress concentrations associated with fastener holes is an added benefit of parts machined out of a single block instead of assembled from many parts. Residual stresses resulting from imprecise assembly are also eliminated. The part's strength and reliability can therefore be increased using HSM techniques.

Another example of Boeing's success using HSM and a good illustration of its advantages is the F/A-18E/F tactical fighter. As a result of implementing HSM, this version of the F-18 fighter is 25% larger than previous versions yet uses 42% fewer parts [24].

The benefits of HSM include:

- drastically reduced lead time
- increased production speeds
- fewer parts to track
- reduced number of suppliers
- higher strength
- reduced weight
- cost savings

This process is more than simply running a machine wide open to crank out parts. There are problems and hardware limitations associated with higher spindle speeds. An important limitation to high speed, high feed machining is forced vibrations. Uncontrolled vibrations of the cutting tool, called chatter, can produce unacceptable surface finishes on parts and can result in broken cutting tools.

### **2.3 Chatter**

Chatter is an unstable forced vibration of the cutting tool during a machining process. Problems caused by chatter include:

- tool breakage and possible personal injury or machine damage
- accelerated tool and machine wear rates
- reduced tolerances on machined parts
- poor surface finish requiring excessive hand-finishing
- increased scrap (from unacceptable products)
- excessive machining noise
- problems machining thin-walled parts

Chatter in milling is caused by the self-excitation of the machine tool. The two main sources of self-excitation in machining as defined by Tlustý [39] are mode coupling and ‘regeneration of waviness’. Mode coupling is a two-dimensional phenomenon that occurs when the tool experiences force feedback in at least two directions simultaneously. Vibrations in these two directions are of the same frequency and have a phase shift that causes an unstable elliptical motion of the cutting tool. Mode coupling is generally associated with orthogonal cutting, as in turning operations. Chatter caused by the ‘regeneration of waviness’ effect (called regenerative chatter) is the important chatter mechanism in milling and is the focus of this thesis. A third cause of chatter is impact dynamics, which occurs at low spindle speeds. Since one chief aim of HSM is to maximize machine spindle speed, this mechanism was not considered.

### 2.3.1 Regenerative Chatter

Regenerative chatter is caused by surface variations associated with previous cuts. As each tool flute passes over the surface of the material and makes a cut, it creates an undulating surface. As the next flute passes and makes a cut, it encounters this wavy surface. If the vibrations of this flute are in phase with the wave left by the previous flute cut, the depth of cut remains constant and the chip produced has a constant thickness. A diagram of this ‘in-phase cut’ is shown in Figure 2.2.

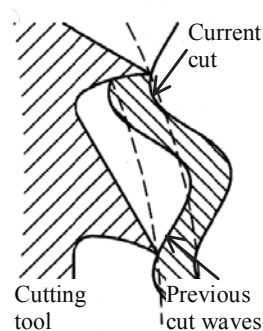


**Figure 2.2: In-phase cut [39]**

During ‘in-phase’ cutting, the cutting force amplitude remains essentially constant and chatter is less likely to occur. If the next flute that passes over the wavy surface vibrates

'out-of-phase' with the surface waves, the thickness of the chip produced is not constant. This 'out-of-phase' cutting is depicted in Figure 2.3

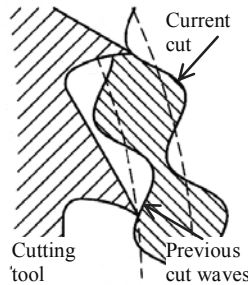


**Figure 2.3: Out-of-phase cut [39]**

In this case, the varying chip thickness creates a varying force on the cutting tool. This harmonic variation in cutting force can result in resonant vibration of the milling tool, or regenerative chatter.

Depth of cut has a significant effect on the vibrational stability of the cutting tool and hence on regenerative chatter. When the cut is shallow, the cutting force amplitudes are small, and cutting is stable at all spindle speeds. The maximum cutting depth that results in stable machining at all spindle speeds is called the limit of stability, denoted  $b_{lim}$ . As will be noted in the next section, certain spindle speeds allow stable cuts at deeper cutting depths. To maximize production, it is desirable to make the deepest cuts possible at the highest spindle speeds possible. These operating conditions will cause chatter unless the previously discussed in-phase tool cuts can be made or the vibrations are controlled and prevented from growing. If machining can be performed in a way that creates in-phase tool vibration, deeper cuts can be made at higher spindle speeds without chatter occurring.

When a cutting tool chatters, the magnitude of vibration causes the tool to lose contact with the workpiece. This loss of contact results in a rough surface finish. This rough finish can require extra hand finishing of the part, or it can exceed tolerances and

requiring scrapping of the part. An extreme example of this rough surface effect is shown in Figure 2.4.

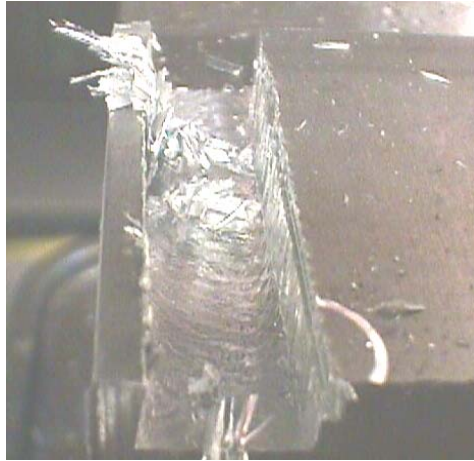


**Figure 2.4: Rough surface finish caused by tool chatter**

### 2.3.2 Stability Lobe Diagrams (SLDs)

Cutting with in-phase tool vibrations can be accomplished by cutting with a flute passing frequency at or near integer divisions of the natural frequency of the cutting tool/spindle/machine system [5]. The flute passing frequency,  $f_f$ , is the tool speed multiplied by the number of flutes. For example, if the spindle speed of a 2-flute tool is 15,000 rpm the flute passing frequency is:

$$f_f = \frac{15,000 \text{ rpm}}{60 \text{ sec/min}} (2 \text{ flutes}) = 500 \text{ Hz} \quad (500 \text{ flute passes per second}) \quad (2.1)$$

Regions of cutting stability lie near these flute passing frequencies. The importance of these stable cutting regions is that cutting depth can be significantly increased [34]. This increase in achievable cutting depth is depicted graphically on a Stability Lobe Diagram (SLD), a plot of stable cutting depth vs. spindle speed. A representative SLD is shown in Figure 2.5.

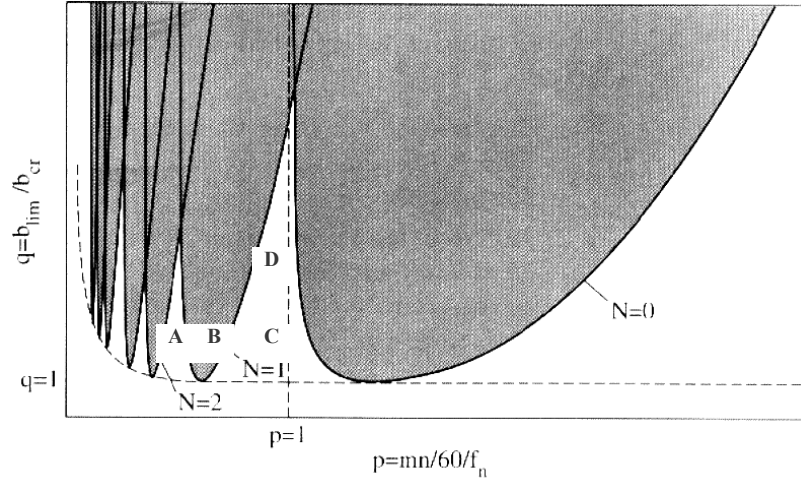


**Figure 2.5: Stability lobe diagram [39]**

The limits of stable cutting depth are delineated with solid lines. Cutting depths above these lines (in the shaded areas) are unstable, while cutting depths below these limits (unshaded regions) are stable. The flat dashed line represents the stability limit cutting depth  $b_{lim}$ , which is the maximum depth a stable cut can be made at all spindle speeds. Analytical derivations of SLDs were developed in the 1960's by Merritt [22], Tlustý and Poláček [38], and Tobias [40]. More recent discussions of stability lobe concepts can be found in Altintas [1], Davies [5], Smith [34], and Tlustý [39].

The frequency response function (FRF) of the tool/spindle/machine system must be accurately known in order to create a SLD. The real component of this FRF generates the stability lobes for regenerative chatter [34]:

$$b = \frac{-1}{2K_s \mu_d \text{Re}(FRF)} \quad (2.2)$$

where:

$b$  = stability lobe boundary (mm)

$K_s$  = specific force of the workpiece material (N/mm<sup>2</sup>)

$\mu_d$  = directional orientation factor

$Re(FRF)$  = real part of the tool/spindle/machine system FRF

The FRF also provides an estimate of the stability limit,  $b_{lim}$  for regenerative chatter [39]:

$$b_{lim} = \frac{-1}{2K_s Re(FRF)_{min}} \quad (2.3)$$

The SLD in Figure 2.5 supports the intuitive reasoning that chatter can be eliminated by decreasing the spindle speed, cutting depth, and feed rate [8]. At very low spindle speeds and feed rates the  $b_{lim}$  limit trends higher, indicating that deep stable cuts can be made at these speeds. This increase in cutting stability at low spindle speeds is the results of process damping [39]. However, the SLD also shows that chatter can be eliminated by increasing the spindle speed to the next higher stability region. Working in these stability regions enables precise cutting (close tolerances) and superior surface finishes with reduced hand-finishing requirements. Since chatter is eliminated, damage to workpiece, tool, and milling machine is eliminated as well. Higher productivity is also a result, since the MRR has not been reduced to avoid chatter. Therefore, accurate prediction of stability regions is a crucial enabling technology for HSM.

## 2.4 Predicting, Identifying and Controlling Chatter

As stated previously, the FRF of the tool/spindle/machine must be accurately known in order to calculate the SLD and determine the optimal cutting conditions. Several chatter avoidance methods discussed in this section use this information to generate stability information. Others rely on real-time measurements to detect and control chatter.

### 2.4.1 Traditional Methods of Chatter Avoidance

The intuitive method of chatter avoidance is to reduce the spindle speed whenever chatter starts to occur. While this method may be effective, it is unnecessarily conservative and

eliminates the potential productivity benefits inherent to HSM. As an example of this technique, suppose a workpiece is being machined at the operating conditions (cutting depth and spindle speed) indicated by point *A* in Figure 2.5. A machine operator may be instructed to increase the spindle speed of the machine to point *B* in order to increase production. This will result in chatter, as the operating point *B* lies in a region of instability. The operator, concerned about damaging the tool and personal injury, will intuitively reduce the spindle speed back toward the original operating point *A*. The SLD indicates that the operator could increase the spindle speed to point *C* instead and reach a stable operating zone, assuming the machine supports this increased speed. Once in that zone, the depth of cut could be increased (at the already increased spindle speed) to point *D*. This point represents a significantly higher MRR than the original operating point *A*.

#### 2.4.2 Modern Efforts to Overcome the Problem

Current and recent efforts to overcome the problem of tool chatter fall into two main categories: *in-situ* control and *a priori* prediction. In-situ methods attempt to sense chatter or its imminent onset and alter the cutting system to avoid it [6, 17, 20]. Predictive methods use experimental or analytical methods to get the frequency response information from the cutting system and avoid chatter. Experimental procedures include exciting the tool with impact hammers [10], explosions [35], and permanent magnets [5]. Analytical approaches include the use of FEA [21] and receptance coupling techniques [4, 29].

#### 2.4.3 In-situ Chatter Control

Research associated with in-situ chatter control involves both identification techniques and control/suppression strategies. Identification techniques involving acoustic signatures [6, 17] and artificial neural networks [20] have been investigated. Chatter control strategies typically involve real-time spindle speed regulation [19, 31, 34]. A possible disadvantage to using these approaches is that they may, by altering the spindle

speed, create fluctuating forces that contribute to instabilities in the cutting process. This may create chatter that would not exist at constant spindle speeds.

Examples of commercial products that use in-situ detection techniques include the Harmonizer [17], distributed by the Ingersoll Cutting Tool Company, and Kennametal's BestSPEED™ analyzer [15, 42]. The Bala-Dyne spindle balancing device [2], while strictly speaking not a chatter-elimination device, can be used to reduce or eliminate spindle vibrations in HSM. This device can be used to reduce or prevent the onset of chatter in machining centers by compensating for excessive spindle vibrations while cutting.

The main problem with in-situ chatter identification and control methods is that chatter has to occur to some degree in order to be detected and reduced in the machining process. This approach is therefore not practical for applications where tolerances or surface finish quality are important. These methods may be acceptable where extensive hand-finishing of parts is expected, though one of the benefits of HSM is the elimination of such work from the machining process. Chatter control methods also require additional CNC components, thereby increasing the cost and complexity of existing machines.

#### 2.4.4 A Priori Chatter Prediction

Several approaches have been used to predict the stability characteristics of milling systems prior to cutting. These include time-domain numerical simulations: detailed dynamic models solved numerically [33, 36] and analytically [1, 23].

Similarly, methods have been used to predict the frequency response of the system. FEA has been used to model and analyze the tool, spindle, and machine bearing system [7, 39]. Receptance coupling theory [4, 29, 30] is another analytical method that has shown promise for predicting the combined vibration response of machine tools, toolholders, and spindles. The frequency response is then used with the analytical solutions to predict chatter characteristics. Modal testing is an experimental approach using either

electromagnetic shakers or impact hammers to excite system dynamics and accelerometers or displacement sensors to measure the response. These traditional vibration testing procedures are discussed in Chapter 3.

Figure 2.6 shows the Ingersoll's chatter analysis flowchart for existing machines [26]. This chart outlines Ingersoll's in-situ and a priori approaches to chatter detection, prediction, and avoidance. This chart presents an iterative process used for chatter avoidance during machining operations that involves adjusting the cutting depth and spindle speed to improve the MRR.

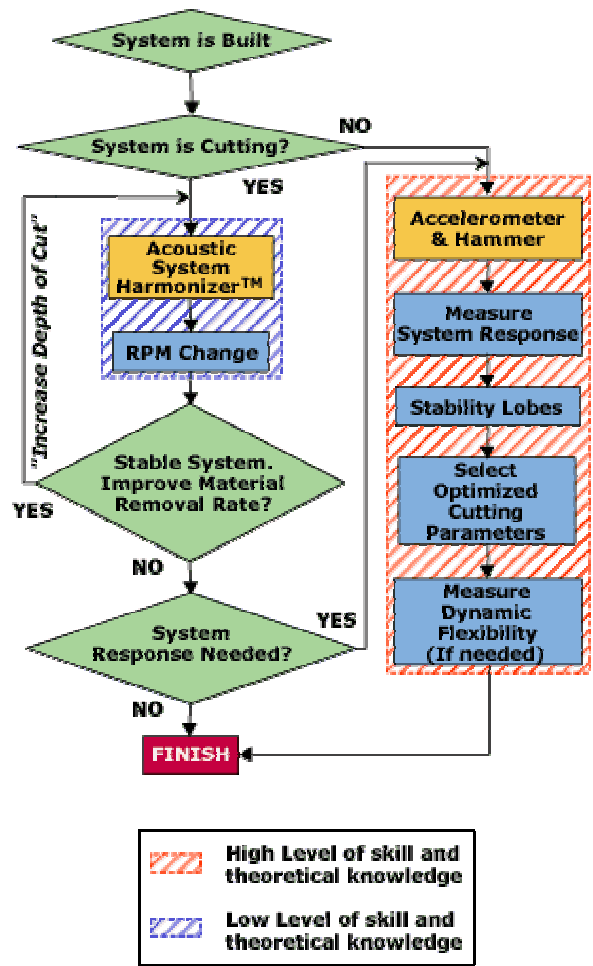


Figure 2.6: Ingersoll's chatter detection flowchart for existing systems (cutting and not cutting) [26]

Ingersoll's experimental methods require technical expertise to perform, while the in-situ chatter detection (acoustic detection) methods require less skill. Acoustic detection techniques use iterative approaches to avoid chatter during the machining process. If the part being machined requires critical tolerances, like an airfoil (e.g. helicopter rotor blade, jet engine IBR,) expensive or irreparable damage may be caused by using this technique unless a test block is used for machine characterization.

There are advantages and disadvantages to both approaches (numerical and experimental) for chatter prediction and avoidance. FEA models have the advantage of giving the FRF at many points on the structure [21]. Also, they can be generalized. However, because FEA modeling does not involve experimental determination of the system FRF, there will be modeling errors associated with manufacturing differences that could be significant. Also, since chatter is driven by single-point forces and interactions at the tool-material interface, a single-point FRF should provide all the information needed for accurate prediction. Finally, the necessity to base FEA models on experimental data raises the question of why experimental methods are not used to produce stability predictions directly.

The main disadvantage of predictive methods (numerical or experimental) is that they generally require technical expertise to perform the necessary tests. Vibration testing using an impact hammer or electrodynamic shaker requires some measure of skill that many machinists and production engineers do not have. Numerical simulations require considerable computing resources, technical expertise, and can be very time-consuming. Expensive, specialized equipment is required for both approaches. Clearly, there is a need for an automated chatter prediction device that is easy to operate, requires no special skills, and gives quick, accurate chatter predictions.

## 2.5 The NIST PM Testing Implementation

Researchers at the National Institute of Standards and Technology (NIST) [5] have devised a passive actuation technique to enable automated prediction of machine tool chatter (Figure 2.7). Their implementation of this technique uses a permanent magnet (PM) to create force excitations on the machine structure. The PM is situated near the tip of the rotating tool to impart magnetic forces as each tooth passes. This creates a train of synchronous excitation forces as the spindle speed is ramped from rest to its maximum speed. This approach simulates the swept sine force profile of an electromechanical shaker, but has the advantage of avoiding mass-loading the tool/spindle/machine structure. The NIST PM implementation also promises the advantage of relatively easy setup and application since no special skills or testing expertise are required. This excitation method is especially beneficial when compared to the impact hammer method for testing tools with longer overhangs where it is particularly difficult to make a clean hit and avoid multiple impacts. Impact hammer testing is discussed in detail in section 3.2.

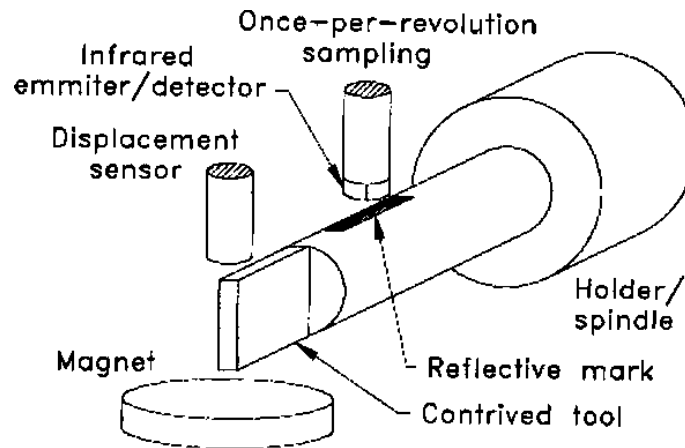


**Figure 2.7: NIST PM passive machine tool actuator [30]**

During experimental demonstrations of the NIST PM device, a capacitance probe and an optical displacement sensor (ODS) were used to sense tool position/deflection. As with the PM, these sensors have the benefit of being non-contacting and not affecting the

system dynamics. To ensure once-per-revolution sampling, a tachometer was used to synchronize displacement sampling with the force input. For testing, a simulated tool was created from a 12.7 mm diameter steel rod with a 10:1 length (overhang) to diameter ratio. The end of the rod was ground flat to simulate tool flutes (see Figure 2.7).

The NIST PM device has a distinct advantage over traditional vibration testing methods in that it requires limited expertise to operate. However, it has operational limitations that prevent it from being universally practical in the manufacturing environment. Its force profiles are not controllable and are limited by the characteristics of the permanent magnet material. Each force profile is shaped passively by the profile of the cutting tool teeth, thus it is not the “clean sinusoid” used in swept sine shaker tests. This introduces unwanted harmonic components into the FRF that could significantly affect the accuracy of chatter predictions. These limitations can be overcome using a controllable electromagnet in place of the PM. This approach is presented in the next section.

## **2.6 Electromechanical Actuation**

The benefits of the NIST PM device for predicting chatter on high-speed milling machines can be expanded using a high-bandwidth electromechanical actuator (EMA). Such an actuator, powered by a controllable current source, could be highly accurate, easy to use, and could become an integral component of a viable chatter prediction system. An electromagnet produces force that is proportional to the square of applied current, and can thus produce larger forces than a permanent magnet. Additionally, the force profile can be precisely controlled by manipulating the coil current. The design, fabrication, and experimental evaluations of such a device are discussed in the following chapters.

### **3 Modal Testing**

Determination of SLDs for HSM applications requires accurate FRF measurements for the tool/spindle/machine system. This section introduces the modal testing techniques and equipment commonly used to obtain system FRFs.

#### **3.1 Overview**

Modal testing is an experimental process used to identify the dynamic characteristics of a structure. Although the underlying theory can be somewhat complicated, modal testing essentially involves three basic steps:

1. Exciting the dynamics of the structure
2. Measuring the excitation and structural response of this excitation
3. Analyzing the response to estimate modal characteristics of the structure

Ideally, the excitation source should input a wide frequency range of energy to the structure, usually in the form of a swept sine or impulse function. The excitation source is normally an electrodynamic shaker or a modally tuned impact hammer. Modal responses are usually measured as accelerations or displacements at various points on the structure. These responses are commonly measured using optical, capacitive, or eddy current displacement transducers or piezoelectric accelerometers.

Data analysis requires data acquisition and signal processing of sufficient bandwidth. Modal analysis can be performed using custom software programs or commercial analyzers specifically designed for testing. These units typically perform FFT analyses and display system responses in the frequency domain.

### 3.2 Impact Hammer Testing

The equipment required to conduct experimental impact hammer tests includes a modally tuned impact hammer, a vibration measurement device, and a two-channel analyzer or data acquisition system. An impact hammer is a specialized piece of modal testing equipment used to excite a structure by emulating an impulse forcing function. A force sensor is attached to the tip of the hammer to provide the force measurement needed for analysis. A pictorial representation of an impact hammer test is shown in Figure 3.1.

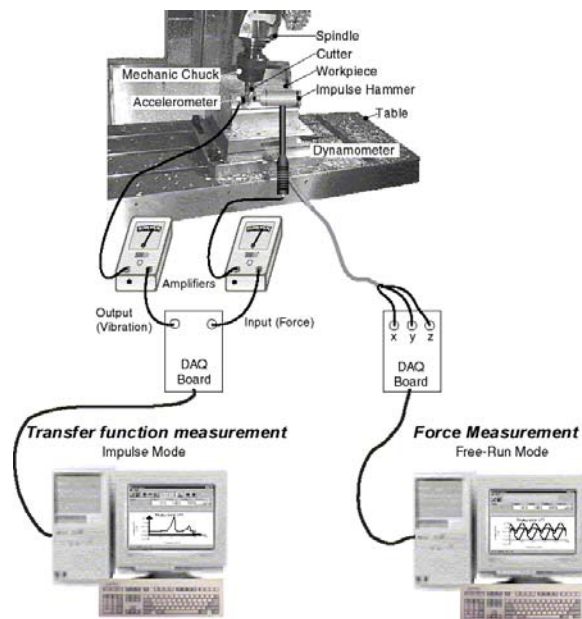


**Figure 3.1: Impact hammer testing for modal analysis [16]**

Theoretically, an impulse input provides infinite amplitude over an infinitesimal time duration, exciting all frequencies in the structure with a constant amplitude. Practically speaking, the hammer will be in contact with the structure for a finite amount of time and will impart a finite force. Considerable skill and technical resources are required to properly perform an impact hammer test. The impact must be ‘clean’ to produce the required broadband excitation. That is, it must be of very short duration and multiple hits or bounces must be avoided. Higher frequency excitation suffers as the pulse width (time

of contact) lengthens. Skill is also necessary to ensure consistent force input. Few machinists or production engineers possess the experience or expertise to make impact hammer testing practical in the machine shop environment.

### **3.3 Shaker Testing**

Although the impact hammer is limited to impulse force profiles, several other inputs are suitable for modal testing. These forcing functions can be produced by a signal generator or analyzer (with the appropriate output capability) and amplified to power an electromagnetic or electrohydraulic shaker. Excitation signals commonly used in modal testing include [10]:

- stepped or swept sinusoids
- random
- impulsive

Stepped and swept sine excitations are similar. A sinusoidal force is applied starting at the lowest frequency of the range of interest and increased throughout the range. The stepped sine excitation, as the name implies is applied in discrete steps with enough resolution to yield meaningful FRF results. The swept sine excitation is increased continually through the frequency range. The suitability of the sweep rate can be tested by comparing measurements taken while sweeping up through the frequency range and then again while sweeping down through the range [10].

One drawback to using shakers on light structures is the addition of mass, which may modify the modal characteristics [21, 27]. The frequency response measured will not reflect the true system dynamics in this case. This could be a significant limitation to the application of shaker testing on machine tools. Shaker tests typically require more sophisticated and expensive equipment (signal generators, power amplifiers, and shakers) than hammer impact tests.

The expertise required to conduct shaker tests is perhaps less than that required for impact hammer tests, but experience is required to set up the tests correctly. Tests can take a long time to set up – as much as an hour or more – which makes this method unfit for use in a production environment.

### **3.4 Non-contacting EMA Testing**

In the production environment, where chatter prediction is crucial, there is seldom an opportunity to properly set up and perform modal tests without creating significant machine downtime. The impact of such tests on productivity is particularly severe for procedures that must be performed every time a tool is changed. Both the shaker and impact hammer approaches to modal testing are inconvenient to use on the shop floor. Not only do they require time to properly set up and execute, they also require considerable skill and experience to conduct. A more straightforward method is needed in order for chatter prediction to be widely practiced.

#### **3.4.1 Benefits of Non-contacting Actuation**

As discussed in Sections 2.5 and 2.6 the benefits offered by the NIST PM implementation and the EMA developed as part of this research include:

- relative ease of use
- reduced test time
- quick and easy set up and removal
- less expensive equipment than is required for other modal tests

Both systems also use non-contacting excitation and measurement technologies, so concerns with mass loading are reduced or eliminated and the system frequency response is not biased or skewed. The NIST implementation uses a capacitive sensor that

necessitates a layer of metallic foil wrapped around the cutting tool tip. The limitations of using a PM to impart the excitation force include:

- limited force amplitudes, even with rare-earth magnets
- non-sinusoidal force profiles
- force profiles are not actively controllable

These limitations can all be overcome by using an EMA in place of the PM. An EMA can deliver a precisely shaped force profile to the cutting tool by manipulating the coil voltage of the device. Integrated software can collect and analyze the input and output data and provide FRFs and time responses within seconds.

The research presented in this thesis focuses on the development and demonstration of a controllable, non-contacting, electromechanical device that is similar in function to the NIST PM device but is better suited to the HSM production environment. Chapters 5 and 6 detail the design and fabrication of this EMA system. An inherent design tradeoff between the achievable force magnitude and bandwidth was managed successfully and a practical device that meets the required specifications was designed and demonstrated. The complete EMA setup consists of the EMA unit (with on-board optical displacement sensing), the control chassis, and a laptop computer (Figure 3.2).

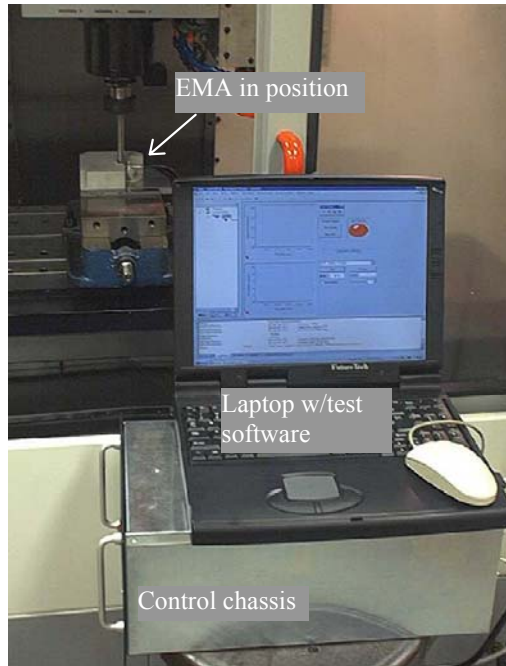


**Figure 3.2: EMA system in test configuration**

The EMA system can be easily operated by someone unfamiliar with typical modal testing procedures. The skills required to operate this equipment and conduct FRF tests are essentially limited to setup and adjustment of cutting tool position relative to the actuator. These are skills widely available on the machine shop floor, making the EMA system well suited to HSM environments.

## 4 Design of the Electromechanical Actuator

Excitation of the milling tool for FRF measurements is accomplished using a specially designed EMA. The electromechanical design of this actuator was developed using magnetic circuit analysis (MCA), and was verified using FEA. This section outlines the simulation-based design process for this actuator.

### 4.1 Design Overview

The primary design objectives for the EMA focused on creating the required force amplitudes and bandwidths to enable accurate FRF measurements for a representative range of machine tools. A common geometry for cutting tools is the helical multi-fluted (flat bottom) end mill. Other HSM tool geometries include ball-nose end mills, cutters with inserts, face mills, slot cutters, etc. Cutting tools can be made of high-speed steel (HSS), tungsten carbides, titanium carbides, cobalt-based alloys, or other materials [8]. The EMA was designed for use with ferromagnetic tool materials, as these provide an ideal path for magnetic flux. The EMA was designed to accommodate a reasonable range of tool sizes, though the design can be revised to function with tools outside this range.

Preliminary design work identified a C-frame electromagnet core with a rectangular cross-section as being optimal for this application (Figure 4.1). A single winding was wrapped around a laminated electrical steel core for this preliminary design. Other core shapes considered included bars, rectangles, and circles. An oval core was chosen because the curved shape minimized leakage fluxes while the straight section provided sufficient length for coil windings. Criteria used to evaluate candidate core designs included maximization of force exerted on the tool, maximization of magnetic flux density  $B$  in the air gap, and minimization of overall actuator size. Angled pole pieces ( $45^\circ$ ) were chosen for their ability to accommodate a range of tool diameters.

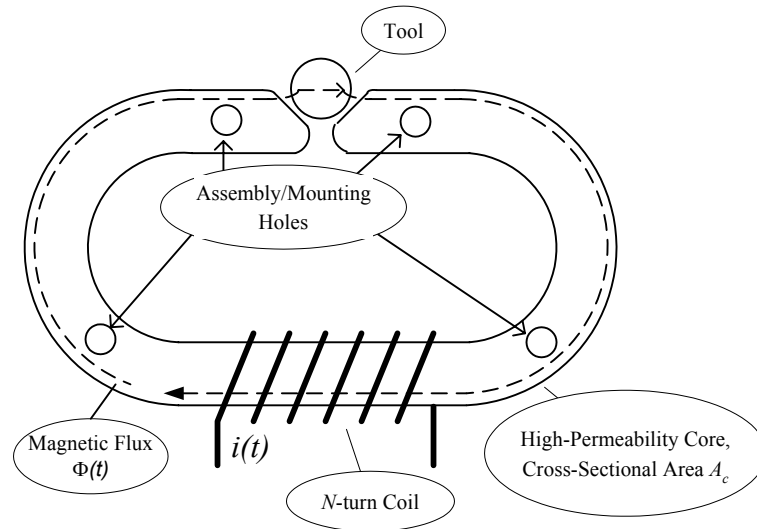


**Figure 4.1: Profile of the electromechanical actuator**

When a high-current excitation signal is applied to the coils, a controllable magnetic flux  $\Phi(t)$  is established in the core and air gap. When a ferromagnetic machine tool is positioned in this air gap, the magnetic flux creates a controllable reluctance force that can be used for FRF excitation. The chief design consideration of the device was the maximization of this magnetic flux in the air gap between the EMA poles and the cutting tool.

The core of an electromagnet must be constructed of a highly permeable material that ‘conducts’ magnetic flux. M-19 laminated electrical steel is an excellent choice for this application. Electrical steel has a relative magnetic permeability approximately 4 orders of magnitude higher than air, so most of the magnetic flux produced in the coils is contained within the core. Tool materials also have high relative permeabilities (3 to 4 orders of magnitude higher than air) so that flux flowing through the core strongly favors a path through the tool when it is inserted in the pole air gap. The air gap creates the only significant reluctance to the magnetic flux in the actuator.

Laminated electrical steel also reduces eddy current losses in the core. Eddy currents are caused by time-varying magnetic fields in electrically conductive materials. They

contribute to the *magnetic skin effect* where alternating magnetic fluxes tend to concentrate on the outside surface of the conductor [32]. Eddy currents create heating and associated power losses in the core. The average power loss per unit volume in a conductor is given by [32]:

$$\bar{p} = \frac{c^2 \omega^2 \hat{B}^2}{24\rho} \quad (4.1)$$

where:

$\bar{p}$  = average power loss per unit conductor volume (W)

$c$  = lamination thickness (m)

$\omega$  = signal (current) frequency (rad/sec)

$\hat{B}$  = maximum flux density (T)

$\rho$  = conductor resistivity ( $\Omega \cdot m$ )

It can be seen from this relation that eddy current power losses are proportional to the excitation frequency, the magnetic flux density, and the square of the lamination thickness. Although any (or all) of these parameters could be reduced to offset power losses, a high-bandwidth, high-force actuator needs high-frequency excitation signals and large magnetic flux densities. Lamination thickness is the only practical parameter to minimize in this design application. For this reason, M-19, a common commercial electrical steel, was selected for this application.

## 4.2 Design Specifications

The required force magnitude was determined from modal testing requirements for a representative range of machine tools and displacement sensors. For a “typical” 4-flute, 4.00” overhang, ½” diameter, HSS end mill, the stiffness was experimentally determined to be  $2.7 \times 10^6$  N/m. This value is well within published ranges of  $6.6 \times 10^5$  to  $7.2 \times 10^6$  N/m [39]. Typical capacitive, inductive, and optical displacement sensors used in similar modal testing applications have resolutions on the order of 0.25 microns. To create measurable tool deflections (0.25 microns) for representative ranges of tools (typical stiffness  $2.7 \times 10^6$  N/m) and sensors, the minimum required force amplitude can be readily calculated:

$$F_{\min} = 2.7 \times 10^6 \text{ N/m} \cdot 0.25 \times 10^{-6} \text{ m} = 0.675 \text{ N} \quad (4.2)$$

To provide a considerable design margin, the peak force requirement was set to ten times this calculated value, or 6.75 N.

As stated in Chapter 3, swept-sine input signals are frequently used in vibration testing because they ensure broadband excitation in the frequency range of interest. Impulse functions also provide broadband excitation, but for highly inductive devices such as the EMA, the voltage required to produce current impulses is prohibitively large. For this application, a swept-sine frequency range of 0 – 1000 Hz was found to sufficiently excite the first mode of a 4.00” overhang, ½” diameter, HSS cutting tool specimen. Based on a cantilever analysis, the first natural frequency,  $f_n$  (Hz), for this cutting tool (approximated as a right circular cylinder) was calculated using the following expression [37]:

$$f_n = \frac{1}{2\pi} \sqrt{\frac{k}{m}} \quad (4.3)$$

where:

$k$  = stiffness constant (N/m)

$m$  = mass (kg)

Approximating this standard tool as a cantilever beam with constant cross-sectional properties undergoing lateral vibration, the following relation can be used for the stiffness coefficient [37]:

$$k = \frac{3EI}{l^3} \quad (4.4)$$

where:

$E$  = Young's modulus of HSS tool = 194 GPa [13]

$I$  = area moment of inertia ( $m^4$ ) =  $\pi d^4/64$  for circular beams

$l$  = overhang length (m)

Combining (4.4) and (4.3) and applying the appropriate boundary conditions provides an expression for the first natural frequency of a laterally vibrating cantilever beam:

$$f_n = \frac{3.52}{2\pi} \sqrt{\frac{EI}{m_l l^4}} \quad (4.5)$$

where:

$m_l$  = mass/unit length of the beam (kg/m)

Using (4.5) the first natural frequency of a 4.00" overhang, 1/2" diameter, HSS cutting tool was calculated to be approximately 750 Hz. This natural frequency can be used to predict the stable machining regions (the SLD) based on the following relation [39]:

$$n = \frac{60f_n}{Nj} \quad (4.6)$$

where:

$n$  = spindle speed (rpm)

$f_n$  = tool natural frequency (Hz)

$N$  = number of flutes on cutting tool

$j$  = integer representing stable cuts

For the 4-fluted, 4.00" overhang, 1/2" diameter HSS cutting tool the stability lobes should occur at:

$$n = \frac{60(750)}{4j} = \frac{11,250}{j}, \quad j = 1,2,3,\dots \quad (4.7)$$

Thus, for HSS tools with length/diameter ratios of 8.0 and higher, an input excitation bandwidth of over 750 Hz is required. The target bandwidth for the EMA was therefore set to 1000 Hz, and the swept-sine excitation signal was set to sweep from 0 Hz to 1000 Hz. Design specifications for the EMA are summarized in Table 4.1.

**Table 4.1: EMA design requirements**

Tool type:	4-flute, flat bottom, helical end mill
Tool dimensions:	3/8" - 5/8" diameter, $\geq 4.00$ " overhang
Tool materials:	Range of ferromagnetic materials from high speed steel (HSS) to tungsten carbide
Force profile:	Swept sinusoids, 0 – 1000 Hz
Force amplitude:	0.0 - 6.75 N
Force bandwidth:	$\geq 1$ kHz

Other requirements for the EMA included manufacturing considerations, namely the ease and cost of manufacturing the actuator and the size of the unit. The EMA has several parts that require machining or forming. These include the actuator core, its mounting base, and its cover. These components must fit together in a package that can be easily clamped into the workpiece holder of any standard milling machine. The fabrication and production details of the EMA are covered in Chapter 5.

### **4.3 Analytical Design and Simulation**

The electromechanical design of the EMA was guided by two analytical techniques: magnetic circuit analysis (MCA) and generalized machine theory (GMT). MCA was used to understand the magnetic flux characteristics of the EMA, and GMT enabled predictions of the force capabilities. An overview of the modeling, analysis, and design using these tools is presented in the sections that follow.

### 4.3.1 EMA Modeling Overview

The actuator dynamics can be modeled using the ‘classical’ iron-core relay with a return spring (Figure 4.2). For this system, a controllable reluctance force,  $F_{em}(t)$ , in the  $x$ -direction can be exerted on the plunger by manipulating the applied coil voltage,  $V_s(t)$ . This voltage establishes a current,  $i(t)$ , in the coils, creating a magnetic flux,  $\Phi(t)$ , in the core, air gaps, and plunger. The reluctance force is resisted by the spring stiffness,  $k$ , creating an oscillatory electromechanical system.

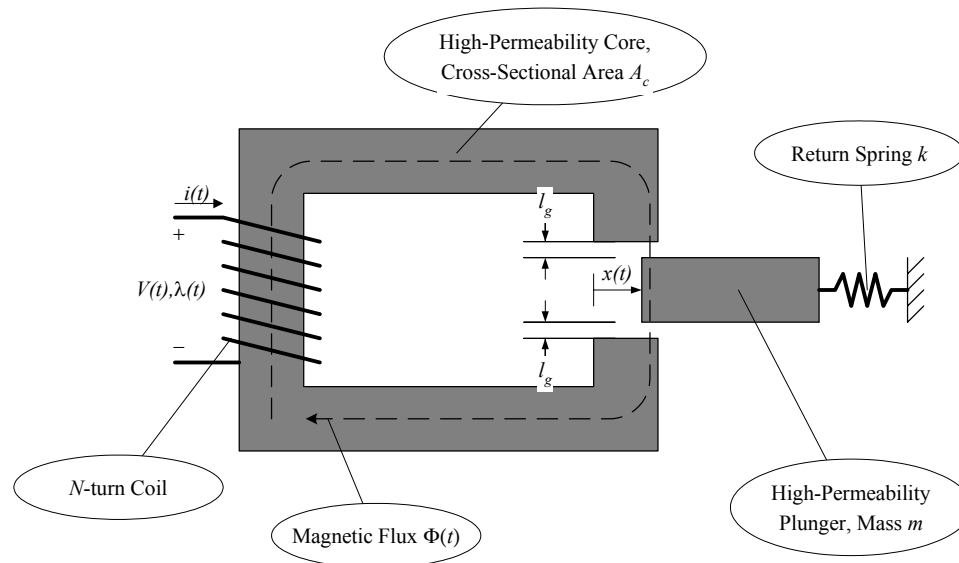


**Figure 4.2: Iron-core relay with return spring**

The cutting tool serves as both the plunger and the return spring. The spring stiffness can be approximated using a cantilevered beam analysis, as summarized in (4.4).

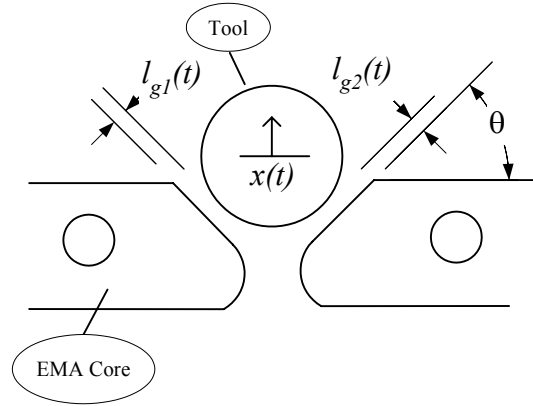


**Figure 4.3: EMA pole configuration**

Based on the EMA pole geometry shown in Figure 4.3, the cutting tool displacement,  $x(t)$ , and the change in the actuator air gap,  $\Delta l_g(t)$ , are related by the following relation:

$$x(t) = \Delta l_g(t) \sin(\theta) \quad (4.8)$$

where  $\theta$  is the pole cutaway angle (in this case  $45^\circ$ ).

#### 4.3.2 Magnetic Circuit Analysis

Magnetic circuit analysis (MCA) is an analytical technique used to model and predict the magnetic flux characteristics of electromechanical systems. This method is based on the direct analogy between electrical circuits and electromagnetic circuits, and replaces electrical components and relationships with electromagnetic equivalents (see Table 4.2).

**Table 4.2: Electrical circuit components and electromagnetic equivalents**

Electrical Component	Electromagnetic Equivalent
Electromotive Force (Volts): $V(t)$	Magnetomotive Force (Amp-turns): $\mathcal{F}(t)$
Current (Amperes): $i(t)$	Magnetic Flux (Webers): $\Phi(t)$
Resistance (Ohms): $R$	Reluctance (Amp-turns/Weber): $\mathcal{R}$

The primary relation used in MCA is Ohm's Law for Magnet Circuits [11], a direct analogy of Ohm's Law for electrical circuits. This equivalent electromagnetic relation states that the magnetomotive force (*mmf*),  $\mathcal{F}(t)$ , required to produce a magnetic flux  $\Phi(t)$  in a circuit is equal to the product of the magnetic flux flowing through the circuit and the equivalent reluctance,  $\mathcal{R}_{eq}$ , of the circuit:

$$\mathcal{F}(t) = \Phi(t)\mathcal{R}_{eq} \quad (4.9)$$

This *mmf* is equivalent to the number of Amp-turns in the coil windings:

$$\mathcal{F}(t) = n_c i(t) \quad (4.10)$$

where:

$n_c$  = number of coils in winding

$i(t)$  = current in coils (A)

MCA, like electrical circuit analysis, has several inherent assumptions that can be critical to the design and interpretation of results. These critical assumptions are briefly outlined in Table 4.3.

**Table 4.3: Critical assumptions of magnetic circuit analysis**

Leakage fluxes are neglected
Fringing fluxes across air gaps are neglected
Magnetic saturation is neglected (magnetic permeability remains constant)
Eddy currents and heating losses in the tool and core are neglected

Additional assumptions related to the specific EMA design problem are outlined in Table 4.4.

**Table 4.4: EMA-specific design assumptions**

The tool remains centered in the actuator gap, $l_{g1}(t) = l_{g2}(t)$ (Figure 4.3)
The tool is ferromagnetic, with a relative magnetic permeability of 4500
The cross-sectional area through the tool (as seen by the magnetic flux) is constant

The magnetic circuit for the EMA is shown in Figure 4.4.

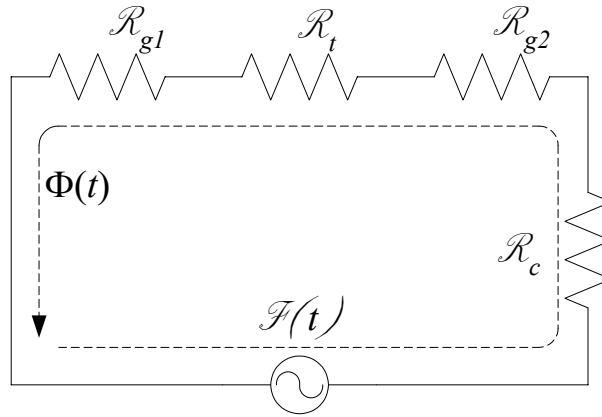


**Figure 4.4: Equivalent magnetic circuit of EMA**

The *mmf* for this actuator,  $\mathcal{F}(t)$ , is created by current,  $i(t)$ , in the coils.  $\mathcal{R}_c$  represents the reluctance of the core material,  $\mathcal{R}_{g1}$  and  $\mathcal{R}_{g2}$  represent air gap reluctances on each side of the tool, and  $\mathcal{R}_t$  is the reluctance of the tool. Each reluctance can be calculated similarly to electrical resistance [9]:

$$\mathcal{R} = \frac{l_i}{\mu A} \quad (4.11)$$

where:

$l_i$  = mean length of the magnetic flux path through the  $i^{\text{th}}$  component ( $m$ )

$\mu$  = relative permeability of the component

$A$  = cross-sectional area of flux path ( $m^2$ )

The four reluctances shown in Figure 4.4 can thus be calculated:

$$\mathcal{R}_{g1} = \mathcal{R}_{g2} = \frac{l_g(t)}{\mu_g A_g}, \mathcal{R}_t = \frac{l_t}{\mu_t A_t}, \mathcal{R}_c = \frac{l_c}{\mu_c A_c} \quad (4.12)$$

As with resistors in electrical circuits, a series of reluctances,  $\mathcal{R}_1, \mathcal{R}_2$ , through  $\mathcal{R}_n$ , has an equivalent reluctance:

$$\mathcal{R}_{eq} = \mathcal{R}_1 + \mathcal{R}_2 + \dots + \mathcal{R}_n \quad (4.13)$$

Combining 4.12 and 4.13 provides an expression for total circuit reluctance in terms of physical EMA parameters:

$$\mathcal{R}_{eq} = \frac{l_c}{\mu_c A_c} + 2 \frac{l_g(t)}{\mu_g A_g} + \frac{l_t}{\mu_t A_t} \quad (4.14)$$

The relative permeabilities of the core and the cutting tool are assumed to be negligible compared to air (i.e. infinite) for this analysis. As a result, the first and third term of (4.14) can be dropped. The equivalent reluctance of the magnetic circuit then becomes:

$$\mathcal{R}_{eq} = \frac{2l_g(t)}{\mu_g A_g} \quad (4.15)$$

Neglecting flux leakage along the flux path, the circuit's flux linkage  $\lambda(t)$  is:

$$\lambda(t) = n_c \Phi(t) \quad (4.16)$$

Combining (4.9), (4.10), (4.15), and (4.16) yields an expression for flux linkage in terms of physical system parameters:

$$\lambda(t) = n_c \left( \frac{n_c i(t)}{\mathcal{R}_{eq}} \right) = \frac{n_c^2 i(t)}{\left( \frac{2l_g(t)}{\mu_g A_g} \right)} = \frac{n_c^2 i(t) \mu_g A_g}{2l_g(t)} \quad (4.17)$$

Since there is initially a nominal gap,  $l_{gnom}$ , between the tool and actuator pole and the tool is moving into the gap by an amount  $-\Delta l_g(t)$ , the actual gap is the difference between the two.

$$l_g(t) = l_{gnom} + \Delta l_g(t) = l_{gnom} + \frac{x(t)}{\sin(\theta)} \quad (4.18)$$

The equation for the flux linkage of the actuator system then becomes:

$$\lambda(t) = \frac{n_c^2 i(t) \mu_g A_g}{2 \left( l_{gnom} + \frac{x(t)}{\sin(\theta)} \right)} \quad (4.19)$$

### 4.3.3 Electrical Dynamics

The electrical circuit can be modeled using Kirchoff's voltage law [11]:

$$V_s(t) - V_R(t) = V_i(t) \quad (4.20)$$

where:

$V_s(t)$  = applied coil voltage (V)

$V_R(t)$  = resistive voltage (V)

$V_i(t)$  = voltage induced by change in flux linkage (V)

The resistive voltage in the coil is determined using Ohm's Law:

$$V_R(t) = i(t)R \quad (4.21)$$

where  $R$  is the total coil resistance, calculated as:

$$R = \frac{\rho l_r}{A_r} \quad (4.22)$$

where:

$\rho$  = resistivity of coil wire ( $\Omega \cdot \text{m}$ )

$l_r$  = coil wire length (m)

$A_r$  = cross-sectional area of coil wire ( $\text{m}^2$ )

The induced voltage is the time derivative of flux linkage:

$$V_i(t) = \frac{d\lambda}{dt} = \frac{\partial \lambda}{\partial i} \frac{di}{dt} + \frac{\partial \lambda}{\partial x} \frac{dx}{dt} \quad (4.23)$$

The first term in (4.23) represents the inductive voltage across the coils, and the second term represents “back emf” or “speed voltage” generated by the moving tool [12]. Evaluating the partial derivatives in (4.23) and combining the results with (4.19) and (4.20) gives the electrical dynamics of the actuator system:

$$\frac{di(t)}{dt} = \frac{V_s(t) - Ri(t) + \left( \frac{n_c^2 i(t) \mu_g A_g}{2 \left( l_{gnom} + \frac{x(t)^2}{\sin(\theta)} \right)} \right) \frac{dx(t)}{dt} + 0}{\frac{n_c^2 \mu_g A_g}{2 \left( l_{gnom} + \frac{x(t)}{\sin(\theta)} \right)}} \quad (4.24)$$

#### 4.3.4 Generalized Machine Theory

The analytical technique used to predict the force capabilities of the EMA, generalized machine theory (GMT), is based on the conservation of energy principle [12]. Electrical and mechanical components are modeled as two-port elements that exchange energy across a lossless magnetic field. The power ports of the electrical terminal are voltage and current, and the power ports of the mechanical terminal are force and position. A block representation of this electromechanical energy conversion element is shown in Figure 4.5.

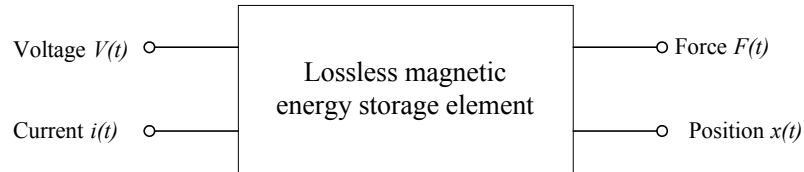


**Figure 4.5: Electromechanical energy conversion element**

Based on the key assumption that the magnetic storage element is lossless, the following energy balance relation [12] is written:

$$\begin{pmatrix} \text{electrical} \\ \text{energy} \\ \text{input} \end{pmatrix} = \begin{pmatrix} \text{mechanical} \\ \text{energy} \\ \text{input} \end{pmatrix} + \begin{pmatrix} \text{increased} \\ \text{magnetic} \\ \text{energy} \\ \text{storage} \end{pmatrix} + \begin{pmatrix} \text{energy} \\ \text{converted} \\ \text{to heat} \end{pmatrix}$$

This relation states that the electrical energy input to the system is either converted to mechanical energy, stored in the magnetic field of the element, or converted into heat. The energy stored in the magnetic field, or another related quantity called co-energy, can be used to derive the EMA output force. The co-energy is defined to be:

$$CoE_f = \int \lambda di = \int Lidi = \frac{Li^2}{2} \quad (4.25)$$

where:

$$L = \text{actuator winding inductance (H)}$$

The actuator force,  $F_a(t)$ , can be calculated from the partial derivative of the co-energy with respect to the air gap,  $l_g(t)$ , holding the current constant [12]:

$$F_a(t) = \frac{\partial}{\partial l_g} CoE_f \Big|_{i=const} \quad (4.26)$$

Combining (4.25) and (4.26) with (4.17) gives the actuator force in terms of physical EMA parameters:

$$F_a(t) = \frac{\partial}{\partial l_g} CoE_f \Big|_{i=const} = \frac{\partial}{\partial l_g} \left( \frac{\lambda(t)i(t)}{2} \right) = \frac{\partial}{\partial l_g} \left( \frac{1}{2} \frac{n_c^2 i(t) \mu_g A_g}{2l_g(t)} \right) \quad (4.27)$$

$$F_a(t) = -\frac{n_c^2 i(t)^2 \mu_g A_g}{4l_g(t)^2}$$

Combining this result with (4.18) produces the final expression for the actuator force:

$$F_a(t) = -\frac{n_c^2 i(t)^2 \mu_g A_g}{4 \left( l_{gnom} + \frac{x(t)}{\sin(\theta)} \right)^2} \quad (4.28)$$

The negative sign in the actuator force expression indicates that this force is always attractive, the actuator can not produce a repulsive force on the cutting tool.

#### 4.3.5 Electromechanical Dynamics

The electrical equations of motion were derived and presented in (4.24). The mechanical equations of motion are derived by applying Newton's second law of motion [12] to the mechanical system of Figure 4.3:

$$m_t \frac{d^2 x(t)}{dt^2} = F_a(t) - F_k(t) - F_d(t) \quad (4.29)$$

where:

$m_t$  = mass of tool (kg)

$F_k(t)$  = spring force of deflected cutting tool (N)

$F_d(t)$  = internal damping force of tool (N)

The spring force of the deflected tool is given by the product of the spring stiffness of the tool,  $k$ , and its deflection,  $x(t)$ :

$$F_k(t) = kx(t) \quad (4.30)$$

The damping force within the tool can be modeled as:

$$F_d(t) = b_s \frac{dx(t)}{dt} \quad (4.31)$$

where:

$b_s =$  system damping parameter (N·s/m)

Combining (4.29) with the force expressions in (4.28), (4.30), and (4.31) yields the mechanical equation of motion:

$$\ddot{x} = -\frac{n_c^2 i(t)^2 \mu_g A_g}{4m_t \left( l_{gnom} + \frac{x(t)}{\sin(\theta)} \right)^2} - \frac{k}{m_t} x(t) - \frac{b_s}{m_t} \frac{dx(t)}{dt} \quad (4.32)$$

The combined electromechanical equations can be expressed in state space form by defining the following phase variables:

$$\begin{aligned} x_1 &= i(t) \\ x_2 &= x(t) \\ x_3 &= \dot{x}_2 \\ u &= V_s(t) \end{aligned} \quad (4.33)$$

The state space representation for this dynamic system is:

$$\dot{x}_1 = \frac{u - Rx_1 + \left( \frac{n_c^2 \mu_g A_g}{2 \left( l_{gnom} + \frac{x_2^2}{\sin(\theta)} \right)} \right) x_1 x_3}{\frac{n_c^2 \mu_g A_g}{2 \left( l_{gnom} + \frac{x_2^2}{\sin(\theta)} \right)}}$$

$$\dot{x}_2 = x_3 \tag{4.34}$$

$$\ddot{x}_3 = - \frac{n_c^2 \mu_g A_g}{4m_t \left( l_{gnom} + \frac{x_2^2}{\sin(\theta)} \right)^2} x_1^2 - \frac{k}{m_t} x_2 - \frac{b_s}{m_t} x_3$$

#### 4.4 Design Parameters

A simulation-based approach was taken to design the electromagnet that is the core of the EMA device. This design was based on a conservative specification of the force required to produce measurable deflection in cutting tools. MCA and GMT performance predictions were used to design the final actuator core geometry. The fabrication of the actuator is discussed in Chapter 5. An example force calculation is presented using the sample data shown in Table 4.5.

**Table 4.5: EMA sample force calculation data**

# coil windings	99
Supply current	5 A
Core depth	1.27 cm
Tool diameter	1.27 cm
Gap (nom)	0.508 mm

One quarter of the tool diameter (1/8") was used as the portion that participates in the force production based on the FEA results discussed in Section 4.5. The force predicted by (4.28) acts perpendicular to the face of the EMA pole. This result is multiplied by  $\sin(\theta)$  to convert it to a lateral tool force:

$$F_a(t) = \frac{-n_c^2 i(t)^2 \mu_g A_g}{4 \left( l_{gnom} + \frac{x(t)}{\sin(\theta)} \right)^2} \cdot \sin(\theta) = \frac{-(99)^2 (5)^2 (4\pi \times 10^{-7}) (1.27 \times 10^{-2})^2 \left(\frac{1}{4}\right)}{4(0.508 \times 10^{-3} + 0)^2} \cdot \sin(45)$$

(4.35)

$$F_a(t) = -8.50N$$

The force predicted by this calculation is slightly conservative since the nominal value of the air gap was used. In actuality, the width of the air gap will be reduced by an amount equal to the force divided by the spring constant of the tool,  $F_a/k$ . An iterative approach can be used to arrive at a more exact prediction, but this was not found to be necessary as the  $F_{min}$  specification included a considerable margin and the difference in force produced caused by the gap change is less than 5.5% for all supply current levels. Results for a range of EMA supply currents appears in Table 4.6.

**Table 4.6: EMA force calculation data**

Supply current (A)	Predicted actuator force (N)
1	0.34
2	1.36
3	3.06
4	5.44
5	8.50
6	12.24
7	16.66
8	21.76
9	27.54
10	34.00

#### **4.5 Finite Element Analysis and Simulation**

Extensive finite element analysis (FEA) was performed on the EMA design to verify the analytical results and make more accurate predictions of the force and flux density capabilities of the EMA design. FEA is more accurate than MCA because the assumptions made to simplify the analysis (Tables 4.3 and 4.4) are not required. FEA requires more computational power than MCA and is therefore a more time-intensive and expensive method of evaluation.

##### **4.5.1 FEMM<sup>®</sup>**

The FEA software used for this actuator was the Finite Element Method for Magnetics (FEMM<sup>®</sup>) package written by Dr. David Meeks. This is a 2D (planar and axisymmetric) analysis software package available free from an internet web site [14]. The software includes graphical pre- and postprocessors, and a solver. The preprocessor allows the user to create drawings or import .dxf files. Analysis results can be displayed and plotted including flux path and density, and various field quantities.

#### 4.5.2 Analysis Setup

The actuator was modeled as an in-plane laminated core made of M-19 electrical steel with a relative permeability of 4416. The coils were modeled as single-turn solid copper conductors with appropriate packing factors applied. These conductors were assigned the relative permeability of copper, 1.0. Current densities in opposing directions were entered for these conductors to simulate current flow in the coil. The material used for the cutting tool was 1117 steel with a relative permeability of 4500.

The FEMM<sup>®</sup> actuator geometry is presented in Figure 4.6. A ½” diameter cutting tool is shown at its nominal position in the EMA pole air gap. The copper coils are represented by the blocks above and below the core in the lower part of the figure.

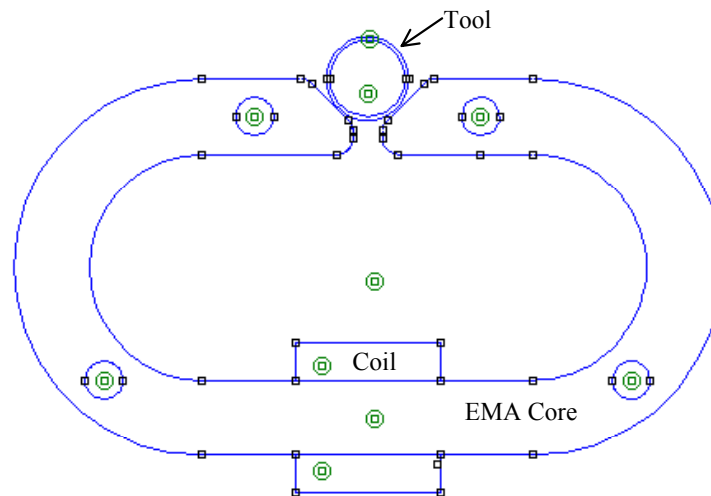


**Figure 4.6: FEMM<sup>®</sup> actuator geometry**

The actuator sections were meshed with triangular elements whose maximum edge sizes are compiled in Table 4.7.

**Table 4.7: FEMM<sup>®</sup> triangular mesh element edge sizes**

Core	0.1”
Coil	0.1”
Cutting tool	0.05”
Air gap	0.01”
Surrounding air	0.1”

The cutting tool and air gap were meshed finer than the rest of the model in order to improve the accuracy of the analysis results in that region. The meshed model is presented in Figure 4.7.

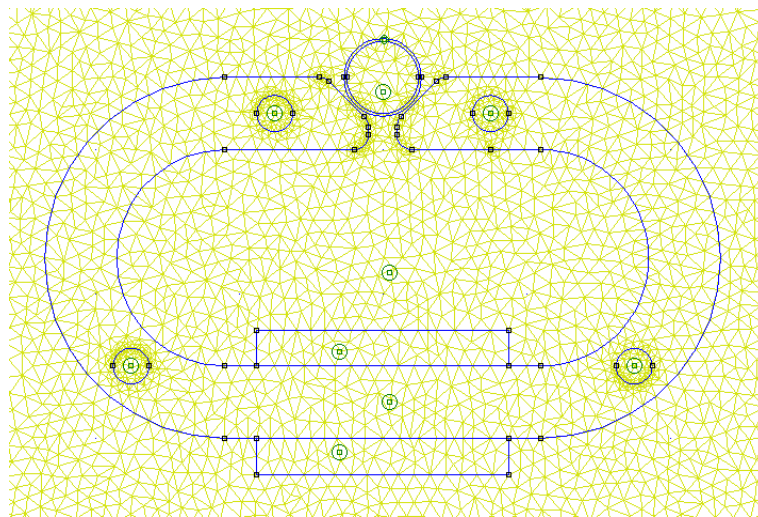


**Figure 4.7: Actuator geometry analyzed with FEMM<sup>®</sup>**

The coil current was specified as bi-directional current densities in the coil blocks. Appropriate current densities were entered for each operating point examined. For example, to simulate EMA operation at a supply current of 5.0 A in the 99 turn coil (an *mmf* of 495.0 Amp-turns), current densities of  $\pm 1.75 \text{ MA/m}^2$  were entered.

#### 4.5.3 FEA Results, Comparison With MCA and GMT Results

The magnetic flux in the EMA is represented in Figure 4.8 by black lines running through the core, across the air gaps, and through the tool. Flux fringing is evident near the air gaps on either side of the tool. Flux leakage is depicted by the lines looping outside the actuator core and around the poles.

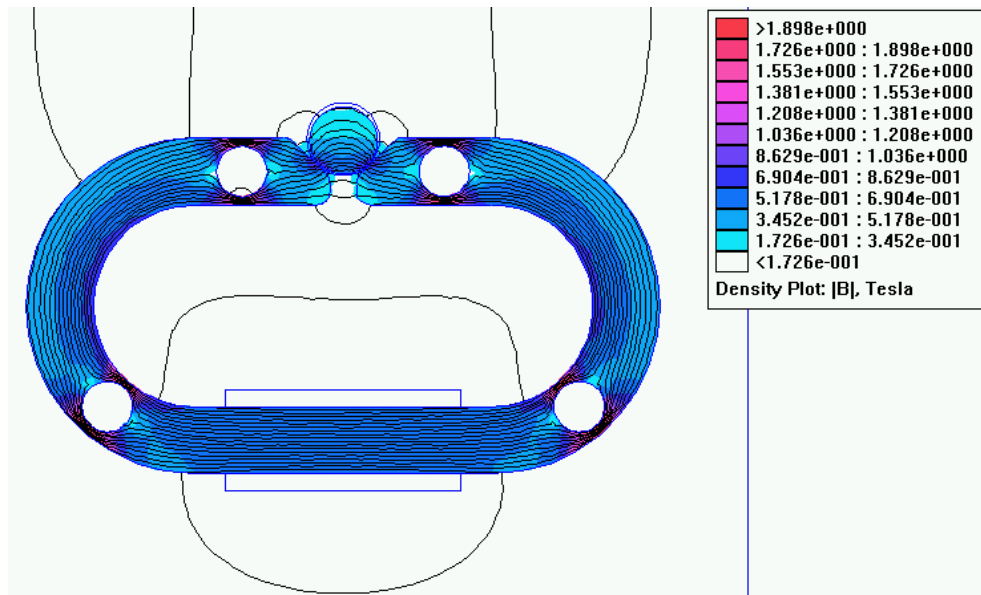


**Figure 4.8: Flux analysis results of the EMA**

The flux lines and flux density levels in the air gaps are shown in greater detail in Figure 4.9. Flux fringing is discernable in this figure.

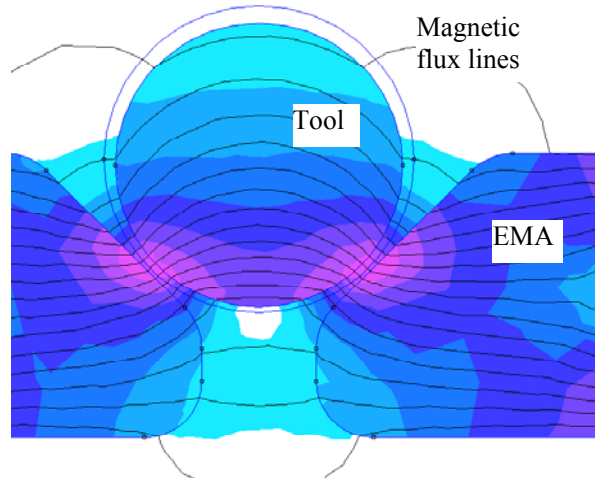


**Figure 4.9: Magnetic flux in the air gaps**

The analytical results obtained using MCA and GMT were compared to the FEMM<sup>®</sup> analysis results and showed very good agreement. The maximum flux density in the actuator air gap in Figure 4.9 is about 0.56 Tesla. The actuation force derived from this flux density in FEMM<sup>®</sup> was 8.7 N for an input current of 5.0 A, which compares almost exactly to the GMT prediction of 8.5 N (4.35). EMA force predictions from FEMM<sup>®</sup> and GMT for a range of EMA coil input currents are presented in Figure 4.10. This figure shows that the actuator forces predicted by the two methods agree up to an input level of 5 A but diverge above this point. This difference is the result of the simplifying assumptions associated with the MCA/GMT analysis method. As discussed in Section 4.3.2 this method assumes there will be no magnetic saturation in the magnetic circuit components. The FEMM<sup>®</sup> results indicate that saturation does occur in the system at coil current input levels above 5 A.

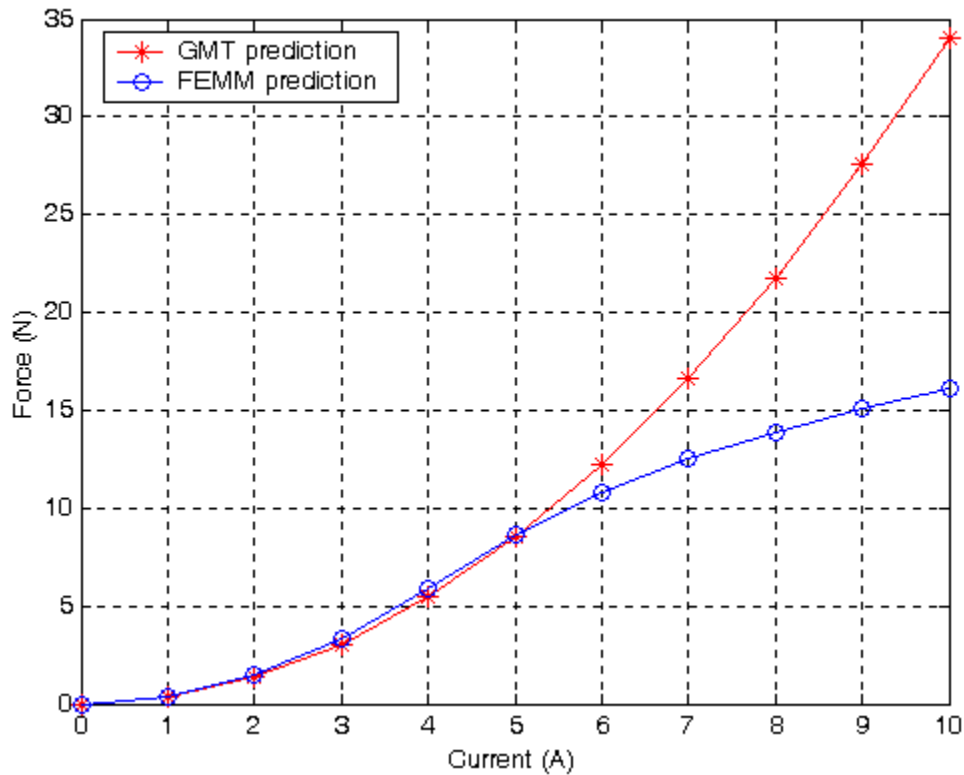


**Figure 4.10: EMA force predictions: FEMM<sup>®</sup> and GMT**

#### 4.6 Design Summary

The design of the EMA was guided by analytical techniques (MCA and GMT) and computational tools (FEA and numerical simulation). These methods predict that the actuator will produce sufficient force to create measurable deflection in cutting tools and enable accurate FRF measurements for a variety of cutting tool materials and sizes.

The analytical predictions made using the two different tools, GMT and FEMM<sup>®</sup> agree (see Figure 4.10). The angled pole pieces allow the actuator to accommodate tools ranging from 1/4" to 5/8". Chapter 6 discusses the successful application of a swept sinusoidal force of 0 Hz to 1 kHz frequency to the tool using the actuator.

## 5 EMA System Hardware

The primary goal of this research was to design, fabricate, and demonstrate the capabilities of an electromechanical actuator (EMA) for use in an automated chatter prediction system for HSM applications. The EMA must deliver non-contacting, high-bandwidth, and properly shaped excitation forces to the cutting tool, which can be rotating or stationary. It must mount conveniently on standard CNC milling machines and readily accommodate a representative range of cutting tools. It must also interface with appropriate data acquisition and control hardware to enable accurate estimation of frequency response functions (FRFs). The fabrication and assembly of the EMA hardware (Figure 3.2 and 5.1) are covered in this section.



**Figure 5.1: Actuator hardware with on-board optical displacement sensor**

### 5.1 EMA Design Overview

As discussed in Chapter 3, a high-amplitude, high-bandwidth electromagnet has several advantages for generating FRFs of tool/spindle/machine systems. Such an actuator, powered by a controllable current source, could be highly accurate, easy to use, and could

become the integral component of a viable chatter prediction system. As outlined in Chapter 4, a C-shaped EMA core was designed with angled poles (Figure 5.2) to accommodate a range of cutting tool diameters. A tool is positioned between the EMA poles with a precise (0.020”) gap on both sides. When a current applied to the EMA coil, the EMA exerts an attractive force on the tool causing a deflection. This is measured using an optical displacement sensor (ODS) on the opposite side of the tool. The force and deflection data is used to generate the FRF of the tool/spindle/machine system.

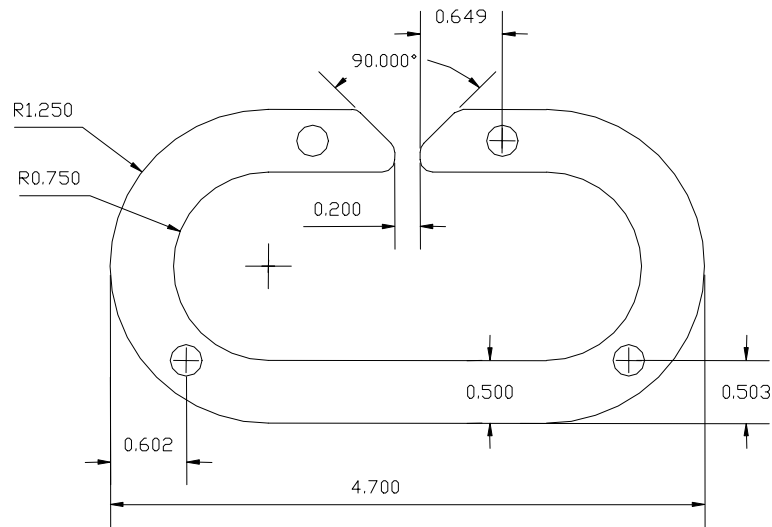


**Figure 5.2: EMA core geometry**

## 5.2 EMA Core

Fabricating the actuator core (Figure 5.3) required careful consideration, as electrical sheet steel is difficult to machine. The processes considered for fabricating the laminations (Figure 5.3) included:

- soft stamping (using a non-hardened die)
- wire electrical discharge machining (EDM)
- laser cutting
- standard milling
- water jet cutting



**Figure 5.3: EMA core laminations**

The soft stamping method of fabrication required that the die be machined (refaced) after every two laminations were stamped. This labor-intensive option was not pursued for obvious reasons. Standard milling processes were evaluated, but machining stacks of steel blanks was time-consuming, labor-intensive, and produced bending and jagged edges that were undesirable. Wire EDM was also evaluated, but was problematic in that the cutting wire bent several blanks during the machining process and did not produce accurate or clean edges. Wire EDM and laser cutting were also among the more expensive alternatives. Water jet cutting was selected for this application because it was relatively inexpensive, gave clean lamination edges, and resulted in quick production turnaround times.

### **5.3 EMA Coil**

As detailed in Section 4.2, a coil was designed to produce the requisite magnetic field. To utilize the full range of the power amplifier ( $\pm 10.0$  A), the coil was designed to carry 10.0 Amps peak. The coil was wound with 99 turns of AWG 16 copper magnet wire in three layers (Figure 5.4). This wire, manufactured by Alpha Wire Company, is rated to 19 A (peak) and specially designed for applications of this type. Protective tape was wrapped around each coil layer to prevent electrical shorts between layers.

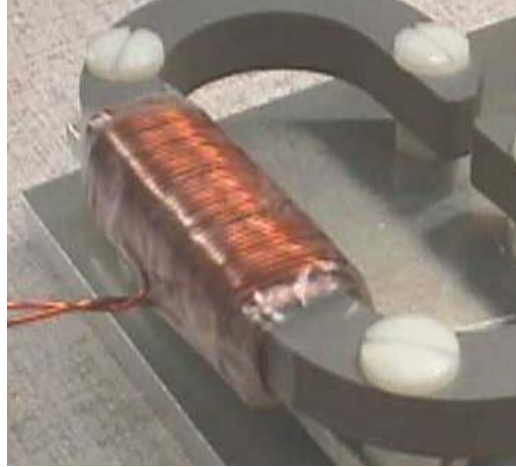


**Figure 5.4: EMA coil**

#### **5.4 EMA Mounting System**

A mounting system was required so that the actuator could be clamped into a standard workpiece vise for testing. The mounting system consisted of a baseplate, a “spider” mounting plate, a force sensor, and the EMA actuator (Figure 5.5). An important consideration in designing the EMA mounting system was that these components should not be ferromagnetic or have high relative magnetic permeability. Ferromagnetic properties would result in significant leakage fluxes from the actuator core, thereby reducing the performance of the EMA. For this reason, the baseplate, spider, ODS mounting post, and EMA housing were all machined from aluminum 6061 T6. Aluminum has a relative permeability of 1.0, meaning it has essentially the same permeability as air.

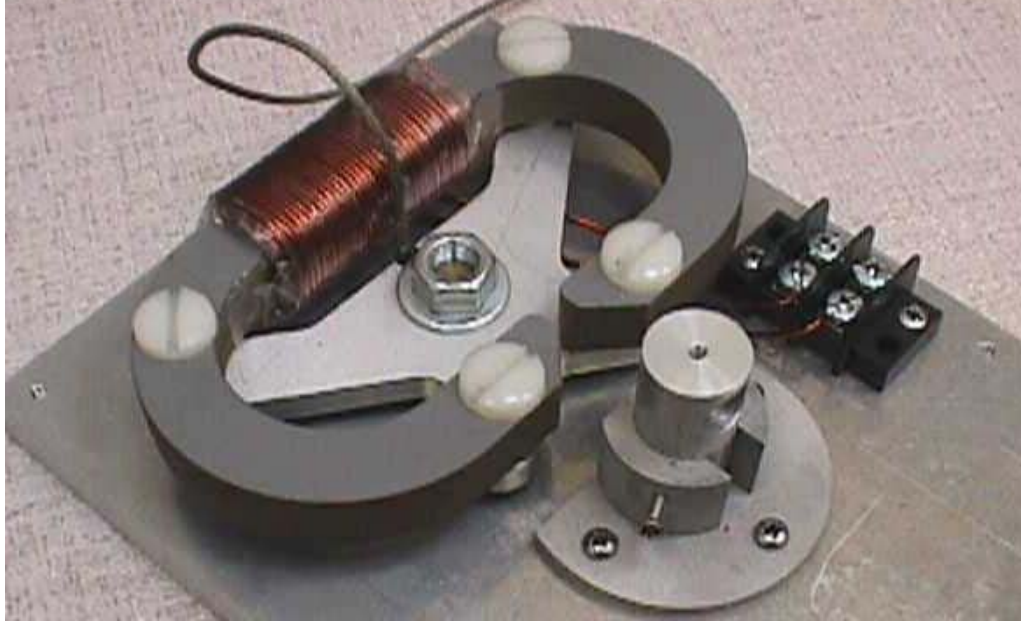


**Figure 5.5: EMA mounting system**

The baseplate (Figure 5.6) was a rectangular plate machined out of ½” aluminum stock. Holes were drilled and tapped for attaching the EMA and ODS support structures.

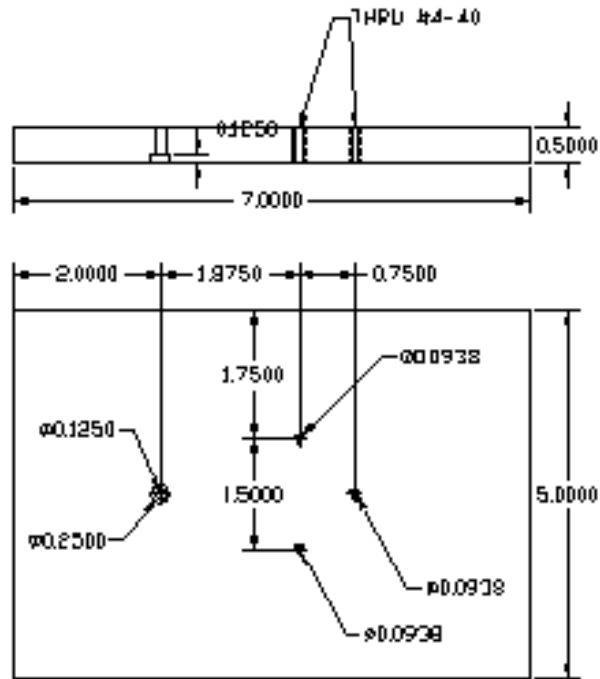


**Figure 5.6: EMA mounting baseplate (all dimensions inches)**

The spider mounting plate (Figure 5.7) was designed to support the EMA through a single mounting point while providing clearance for the EMA coils. The single mounting point enabled force measurements using a washer-style load cell (the PCB 201M73). The EMA core was hard-mounted to the spider mounting plate via four threaded fasteners.

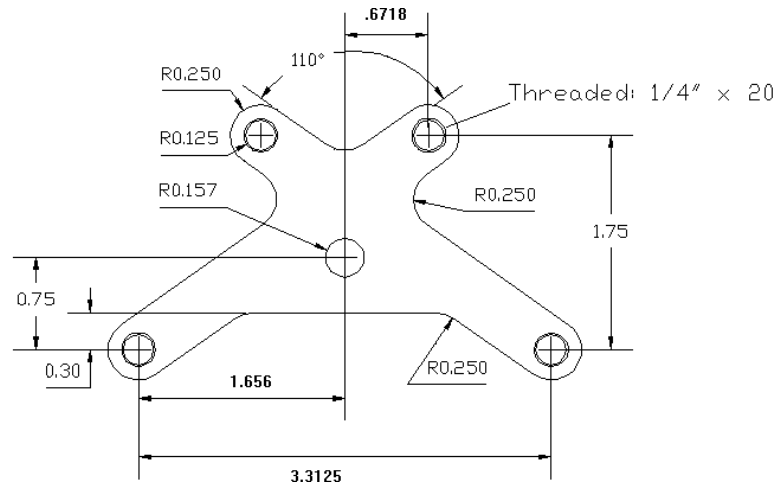


**Figure 5.7: EMA spider mounting plate (all dimensions in inches)**

This spider was bolted to the actuator baseplate through a washer-style load cell. The baseplate was rigidly clamped into the workpiece vise during testing (Figure 5.8).

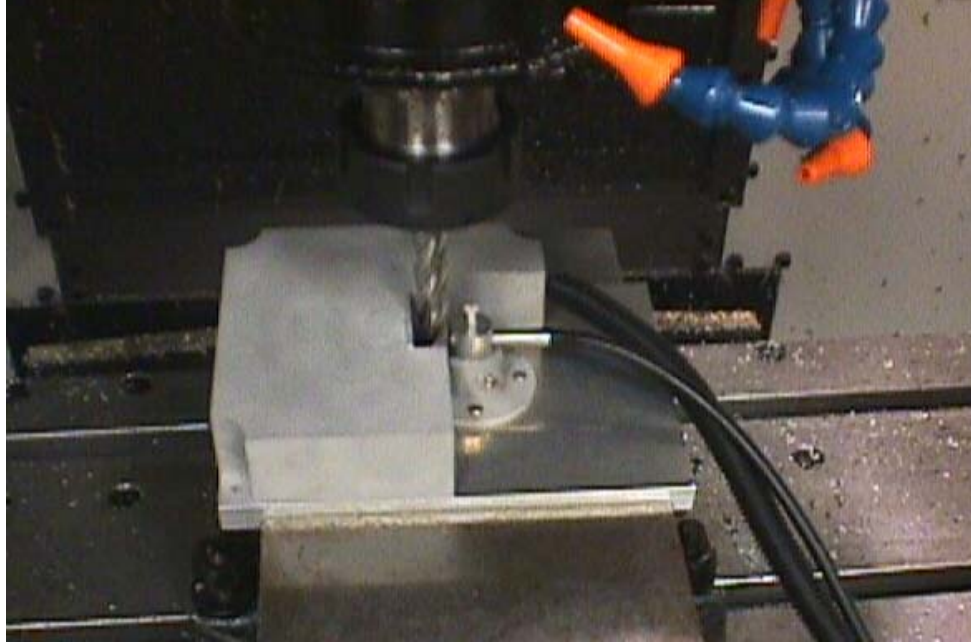


**Figure 5.8: EMA baseplate clamped in workpiece vise for testing**

A PCB 201M73 unidirectional shear (washer configuration) force sensor was used to measure dynamic forces produced by the actuator. This was a custom-designed unit with a measurement range of 100 lbf (0.4448 kN) and a resolution of 0.002 lbf (0.009 N.) The calibration curve (provided by the manufacturer) for this sensor is shown in Figure 5.9.

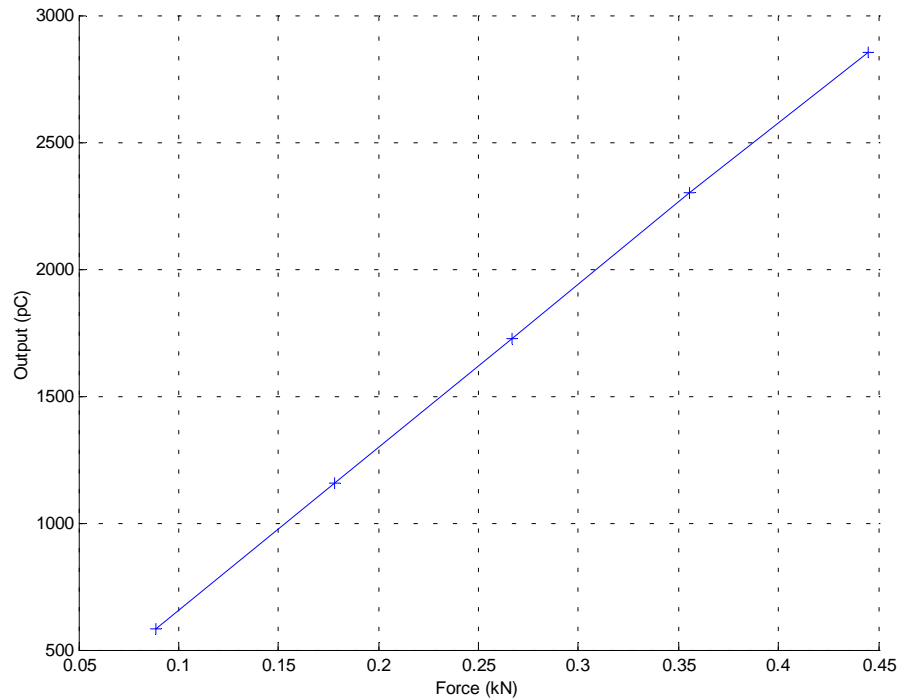


**Figure 5.9: PCB 201M73 calibration curve**

The force sensor has a charge output. This sensor was used in combination with a PCB 422M98 charge converter, which has a sensitivity of 0.5063 mV/pC.

### 5.5 Optical Displacement Sensor and Mounting Post

A Philtec RC25 reflectance-compensated ODS was used to measure the cutting tool displacements. This sensor has a measurement range of 0.8 mm and resolution of 0.25  $\mu\text{m}$ . The RC25 is ideally suited for this application not only because of its specifications, but also because the sensor tip is small (7.137 mm dia.) and the amplifier module is compact (10.8 cm x 6.71 cm). Table 5.1 and Figure 5.10 provide complete specifications and calibration curves (provided by the manufacturer) for this sensor, respectively.

**Table 5.1: Philtec RC25 output specifications**

Range:	0.8 mm
Standoff:	0.36 mm
Linear Range $\pm 1\%$ :	0.2 mm
Sensitivity:	110 mm/mV
Resolution DC - 20 kHz:	0.25 $\mu\text{m}$

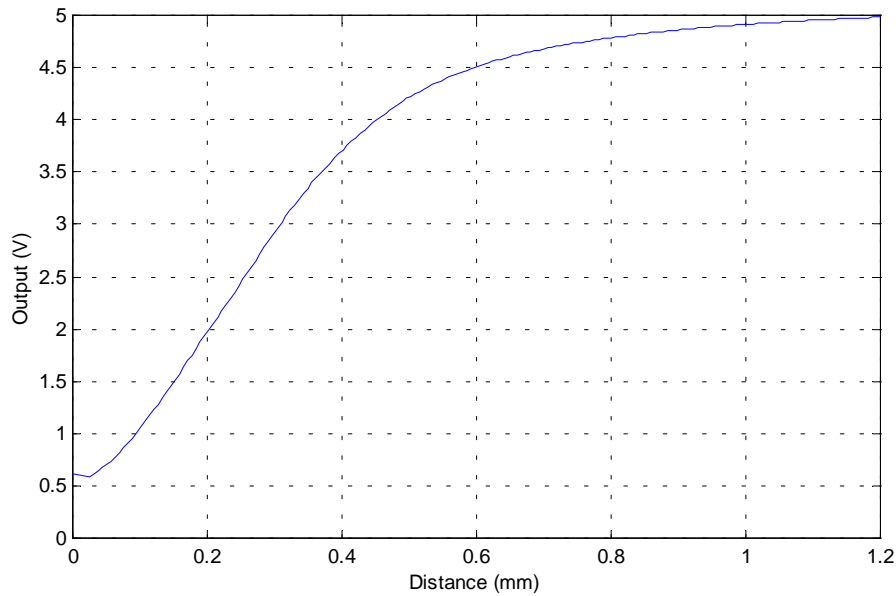


**Figure 5.10: Philtec RC25 calibration curve**

An adjustable mounting system was designed for the ODS (Figure 5.11). The vertical sensor post is adjustable in height, while the sensor's lateral insertion is adjustable to accommodate different cutting tool diameters and provide clearance for gap adjustment. Both adjustments have set screws to prevent sensor motion during data collection. Drawings of the ODS support and adjustment post are presented in Figure 5.12.



**Figure 5.11: ODS support and adjustment insert post**

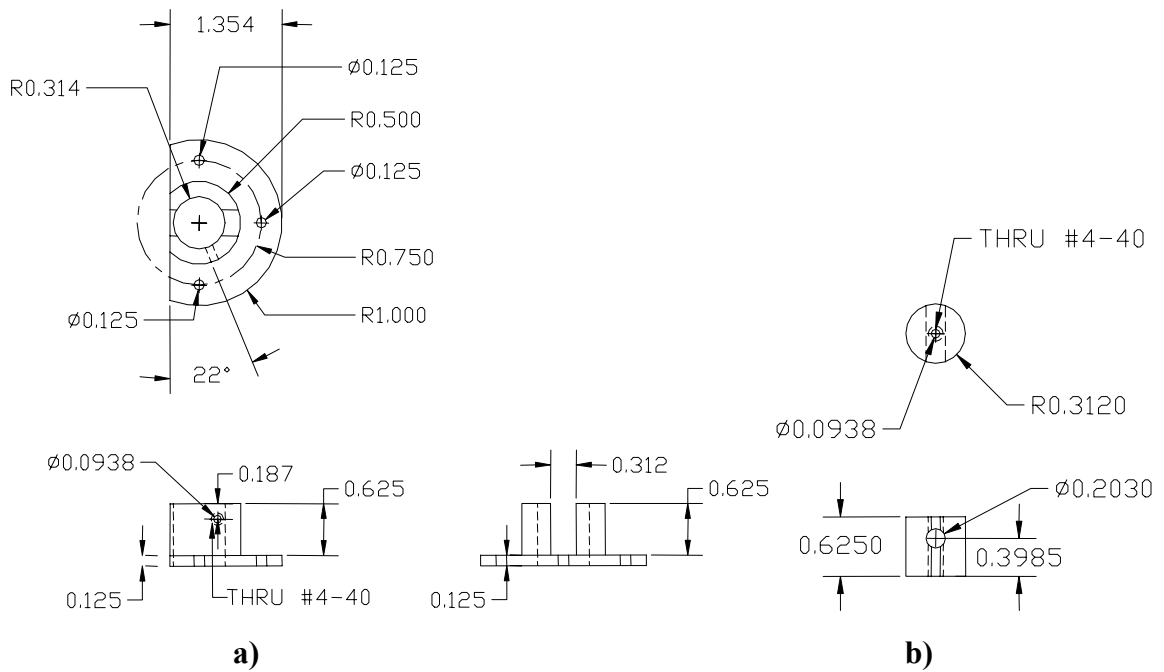


**Figure 5.12: ODS a) base and b) adjustment sensor post (all dimensions inches)**

## 5.6 EMA Housing

An aluminum housing was designed to cover the actuator, protect it from debris and cutting fluids, and provide for easy tool alignment. A drawing of this EMA housing is shown in Figure 5.13. A photograph of the housing appears in Figure 5.1.

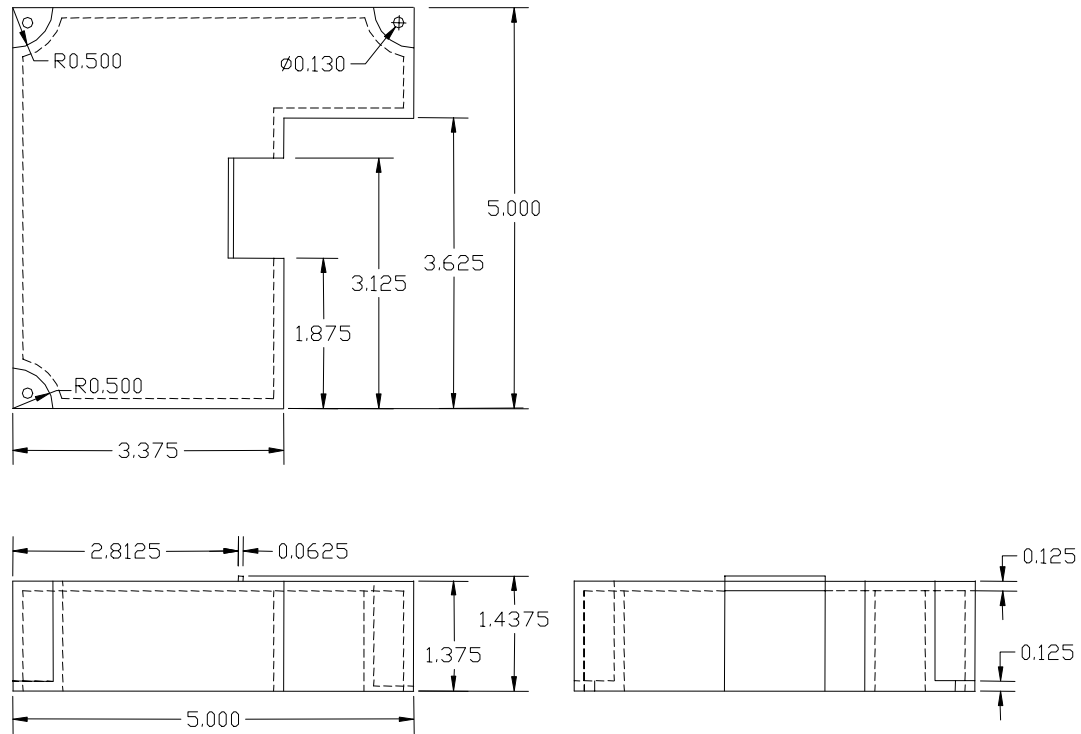


**Figure 5.13: EMA housing (all dimensions inches)**

## 5.7 Real-time Control Chassis

A dSPACE<sup>®</sup> (digital Signal Processing And Control Engineering) 1102 ACE kit was selected for real-time data acquisition and system control. This hardware platform was programmed using Simulink<sup>®</sup> and the Real Time Workshop<sup>®</sup>, which interface with dSPACE's real-time hardware to form an integrated development and testing environment. Synchronous swept sine actuation and displacement measurements were programmed using Simulink<sup>®</sup> and implemented on the dSPACE<sup>®</sup> platform. Figure 5.14

shows the highest level of the Simulink<sup>®</sup> data acquisition and control program. Sine wave and sweep timing functions are performed in subsystems.

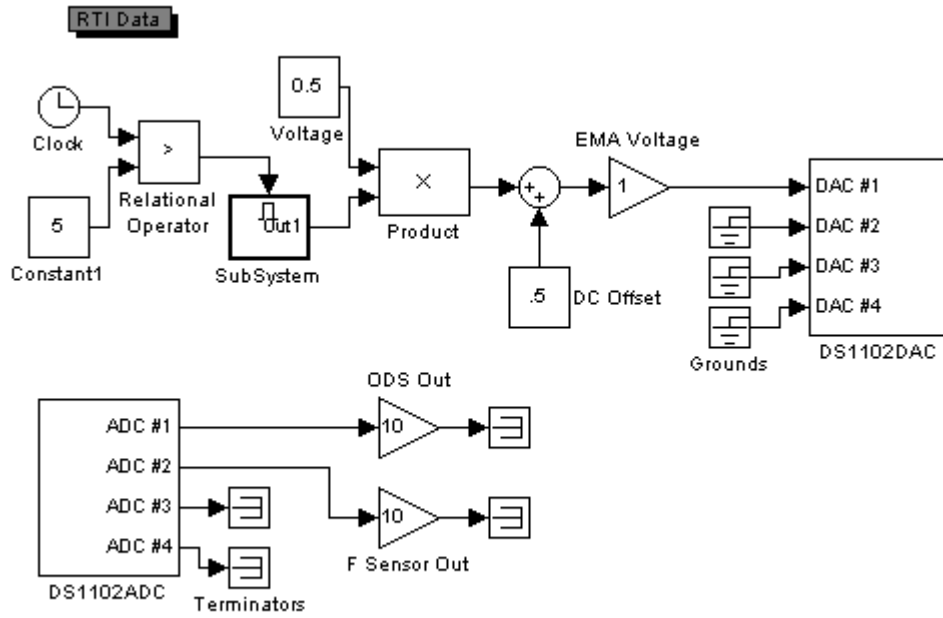


**Figure 5.14: Simulink<sup>®</sup> real-time data acquisition and control program**

The control hardware was housed in an external chassis that linked to a laptop PC via a high-speed serial connection. The link used two serial communication cards, one in the laptop and one in the control chassis. The interior of the control chassis is shown with components annotated in Figure 5.15.

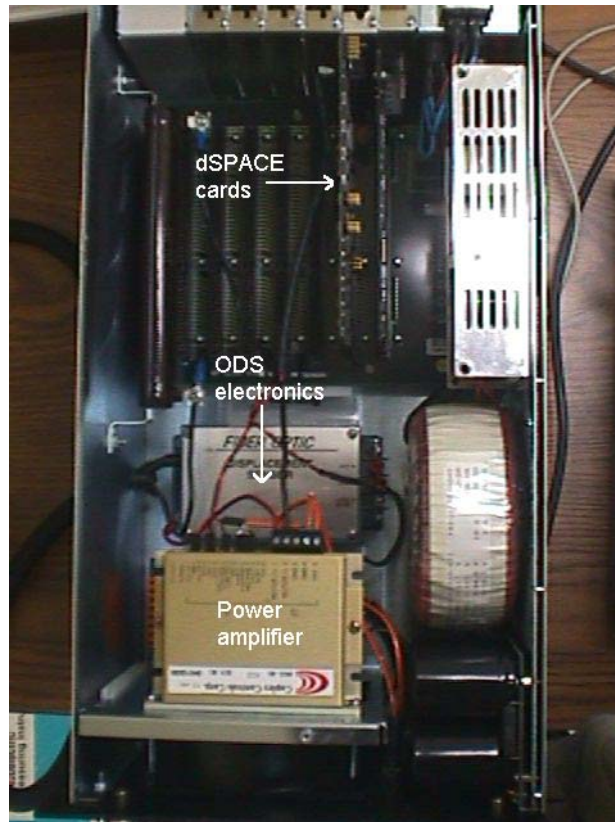


**Figure 5.15: Real-time control chassis interior**

## **6 Experimental Evaluations**

Extensive experimental tests were conducted using a variety of tools and operating conditions to verify the analytical and simulated performance of the EMA. The goal of these tests was to validate the feasibility of the EMA as one component of a chatter prediction and avoidance system for HSM applications. The details of these experimental validations are presented in this section.

### **6.1 Test Objectives**

The specific objectives of these experimental validations were threefold. First, tests were conducted to verify the actuator amplitude and bandwidth predictions derived using analytical methods: MCA and FEA. EMA flux and force characteristics were evaluated for a variety of tool materials, tool sizes, input current amplitudes and waveforms. The second objective was to compare FRFs produced using the EMA to those obtained using a traditional vibration testing method - impact hammer testing. To that end, tests were conducted on stationary (non-rotating) and rotating tools and blanks of various materials and dimensions. Finally, tests were conducted to demonstrate the ultimate utility of the EMA device as part of an automated chatter prediction system: to validate regions of chatter and stable cutting predicted using EMA data. The following sections summarize these experimental validations.

### **6.2 Verification of EMA Flux Characteristics**

Initial experiments focused on verifying the magnetic flux densities produced by the EMA. These results were compared to predictions obtained from FEMM<sup>®</sup> analyses. These FEMM<sup>®</sup> analyses included factors that simulated magnetic saturation in the EMA core. Flux density measurements were made using a Magnetic Instruments gaussmeter (model 912) with a Hall effect probe. Measurements were taken between the poles of the actuator, with no ferromagnetic tool in the gap. A comparison of predicted and measured air gap flux density vs. the applied magnetic field,  $H$ , is shown in Figure 6.1. The

experimental measurements compared favorably with FEA results (obtained using FEMM<sup>®</sup>). The upper and lower limits of flux density variations predicted using FEA are represented by red lines in the figure (measurements depend on probe location in the air gap).

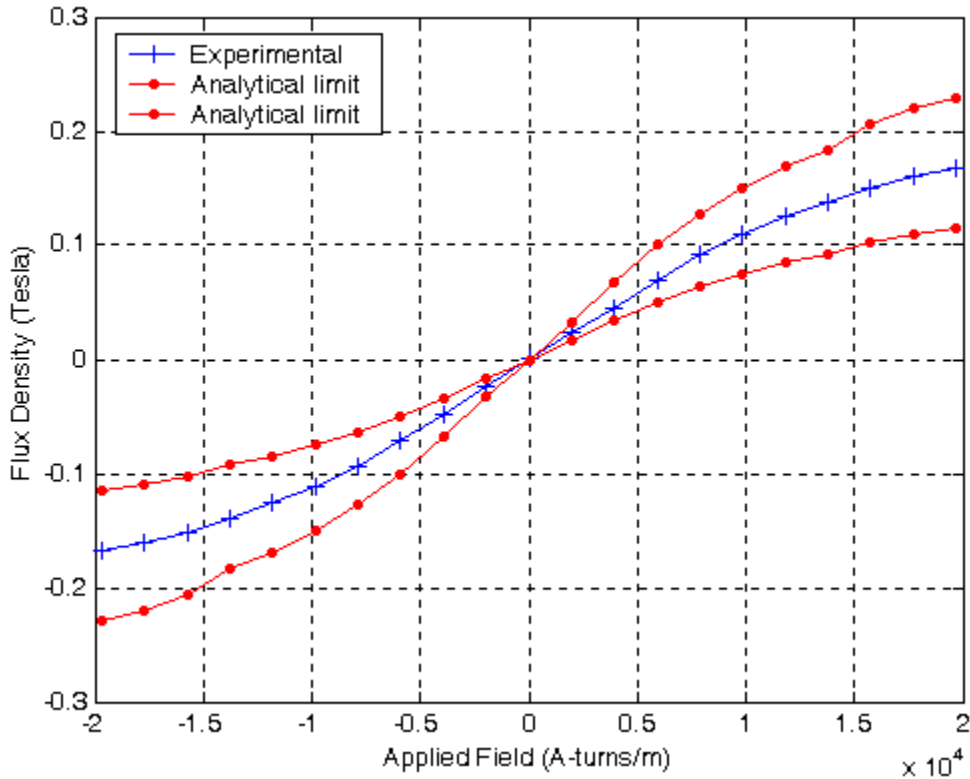


**Figure 6.1: Experimental measurements and FEA predictions of EMA flux density vs. applied magnetic field**

### 6.3 Verification of EMA Force Characteristics

Experimental force measurements were taken using a Kistler 9251 3-axis piezoelectric load cell and a PCB 201M73 single-axis quartz force ring for comparison to static and time-varying FEA predictions. For these tests, a ½” diameter tool steel blank was chucked into a Haas VF-1 5-axis vertical machining center and positioned between the EMA poles to achieve nominal air gaps of 0.02”. The overhang length of this blank was

very short (only 1.00”) so that tool deflections would not affect the air gap dimensions. FEMM<sup>®</sup> predictions of force amplitude for different input currents are displayed in Figure 6.2, along with experimental measurements for the same conditions. The measured force amplitudes match the FEA predictions for a range of input currents up to about 3.0 A. The deviations between measured and predicted forces above 3.0 A are clearly the result of excessive saturation in the core material, and seem to indicate that the electromagnetic properties of the laminated electrical steel differ from published values. Despite this excessive saturation condition present at higher currents, the EMA produces more than the required peak force of 6.75 N.

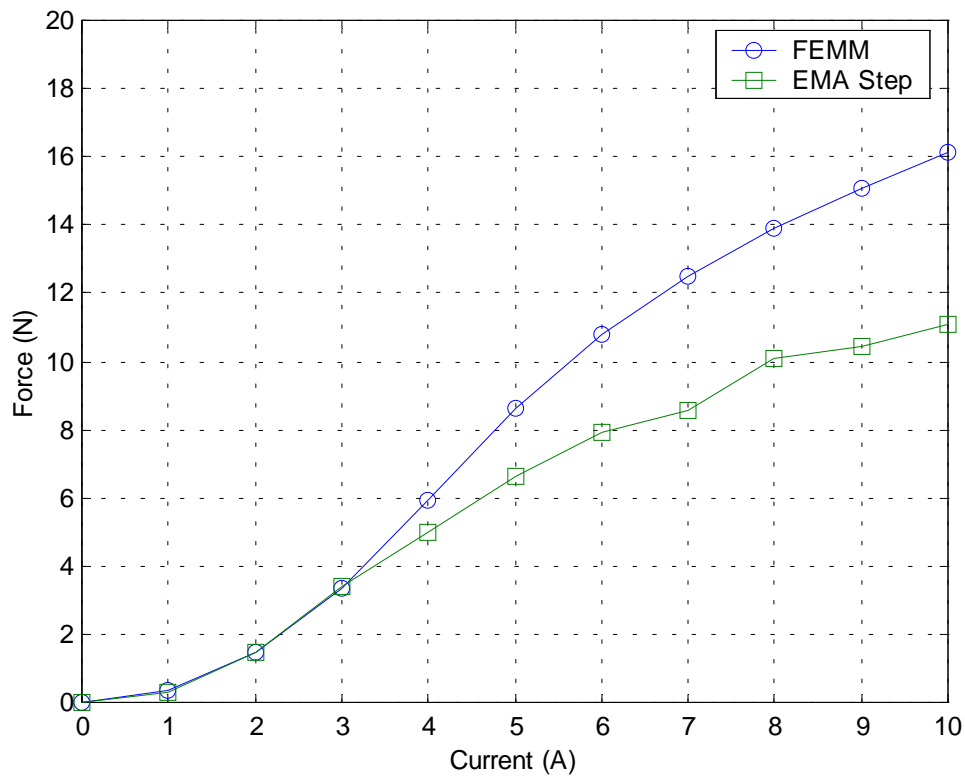


**Figure 6.2: Experimental measurements and FEA predictions of EMA force amplitude**

## 6.4 EMA Modal Tests

The ultimate utility of the EMA device lies in its ability to predict stable machining regions for HSM applications, which requires accurate FRF measurements of the tool/spindle/machine system. For this reason, extensive modal testing was conducted using the EMA on a variety of tools and tool blanks mounted on a Haas VF-1 5-axis vertical machining center. The objective of these tests was to verify the dynamic operation of the EMA and the accuracy of the FRFs it produced. These FRF experiments were performed in two phases. The first phase involved FRF measurements on non-rotating tools, with results being compared to those produced by impact hammer tests. The second phase of experimentation involved FRF measurements on rotating tool blanks. The purpose of these experiments was to test the real-time pulse shaping capabilities of the EMA. Both phases of EMA modal testing are detailed in the following sections.

### 6.4.1 EMA Modal Tests: Non-Rotating Tools

The baseline operation of the EMA must be verified to validate the feasibility of using it as part of a HSM chatter prediction system. The FRF results should compare favorably to those produced using traditional modal testing methods, namely impact hammer tests. The first phase of EMA modal testing was limited to non-rotating cutting tools and blanks because impact hammer testing cannot be performed on rotating tools.

The experimental EMA hardware configuration was detailed in Chapter 5. This system includes the prototype actuator, the control chassis, and the laptop computer with the operational software installed. A photograph of this hardware configured for testing on the Haas VF-1 5-axis vertical machining center is shown in Figure 3.2.

The tool specimens were securely mounted in the toolholder with precisely measured overhangs. Tool blanks (2.00”–6.00” in length) were fabricated from ½” diameter sections of steel drill rod. Drill rod was selected because of the need for high dimensional tolerances and minimal runout. The EMA baseplate was mounted securely

in a workpiece vise and the position of the tool specimen (with respect to the EMA poles) was adjusted until both nominal air gaps measured precisely 0.02". A high-resolution ODS, model RC25 from Philtec, was positioned with a nominal air gap of 0.01" between the sensor face and the tool specimen.

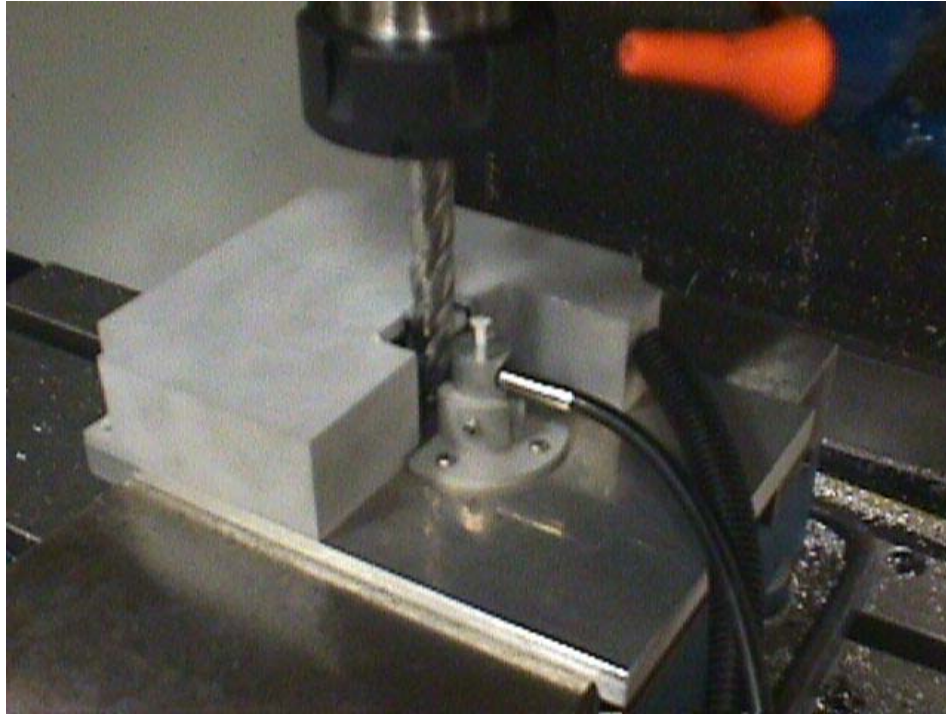


**Figure 6.3: Closeup of actuator in test position**

For reasons discussed in Section 3.3, EMA modal tests employed a swept-sine current input applied to the actuator coil. The frequency of this current input was varied linearly from 0 Hz to 1 kHz in 30 seconds. A 30-second sweep time was determined to provide accurate and repeatable results while maintaining manageable data file sizes and capture times. Real-time data acquisition and control were facilitated using dSPACE<sup>®</sup> 1102 hardware and software operating at a 5 kHz sampling rate. For each FRF test, the swept current profile was generated by the dSPACE<sup>®</sup> system, amplified by a Copley Controls 4122 power amplifier, and applied to the EMA coil. The tool's displacement response was measured using the Philtec RC25 optical displacement sensor and recorded for future FRF processing. Immediately following each EMA test, impact hammer tests were

conducted to prevent discrepancies in the FRFs caused by minor differences in tool length or chucking torque. A summary of experiments conducted is presented in Table 6.1.

**Table 6.1: EMA modal testing summary for non-rotating specimens**

<b>Tool</b>	<b>Overhang Length</b>	<b>Spindle Speed</b>	<b>Excitation Source</b>	<b>Excitation Profile</b>	<b>Excitation Sweep Range</b>
cylindrical blank	6.00"	0 rpm	EMA	Sweep	0 Hz - 1 kHz
cylindrical blank	6.00"	0 rpm	Hammer	Impulse	N/A
cylindrical blank	4.00"	0 rpm	EMA	Sweep	0 Hz - 1 kHz
cylindrical blank	4.00"	0 rpm	Hammer	Impulse	N/A
cylindrical blank	2.00"	0 rpm	EMA	Sweep	0 Hz - 1 kHz
cylindrical blank	2.00"	0 rpm	Hammer	Impulse	N/A
4-flute end mill	3.50"	0 rpm	EMA	Sweep	0 Hz - 1 kHz
4-flute end mill	3.50"	0 rpm	Hammer	Impulse	N/A

Typical FRF tests results for tool blanks with 4.00" and 6.00" overhangs are presented in Figures 6.4 and 6.5, respectively, with impact hammer data in red and EMA data in blue. Note that the hammer results represent an average of 10 consecutive tests. Although the EMA data is somewhat noisier than the impact hammer data, the modal characteristics (magnitude and frequency) are very similar. For the 4.00" overhang tests, the first natural frequencies determined from these tests are 747 Hz for the EMA and impact hammer. For the 6.00" overhang tests, the first natural frequencies are 347 Hz and 350 Hz for the EMA and impact hammer, respectively.

Small discrepancies in natural frequency can be attributed to variations that result from impact hammer testing. Repeated impact hammer tests on the same specimen, even with spectrum averaging, resulted in variations in modal peak location of up to 20 Hz. This variation is equivalent to a 600 rpm range of uncertainty in the predicted location of a stable cutting speed on the SLD for a 2-fluted tool and a 300 rpm range in the predicted

location of stable cutting region for a 4-fluted tool. These results highlight the variance that can come from impact hammer tests, especially on asymmetrical objects like helical fluted tools, and underscore the fact that hammer testing requires some skill to perform properly and consistently.

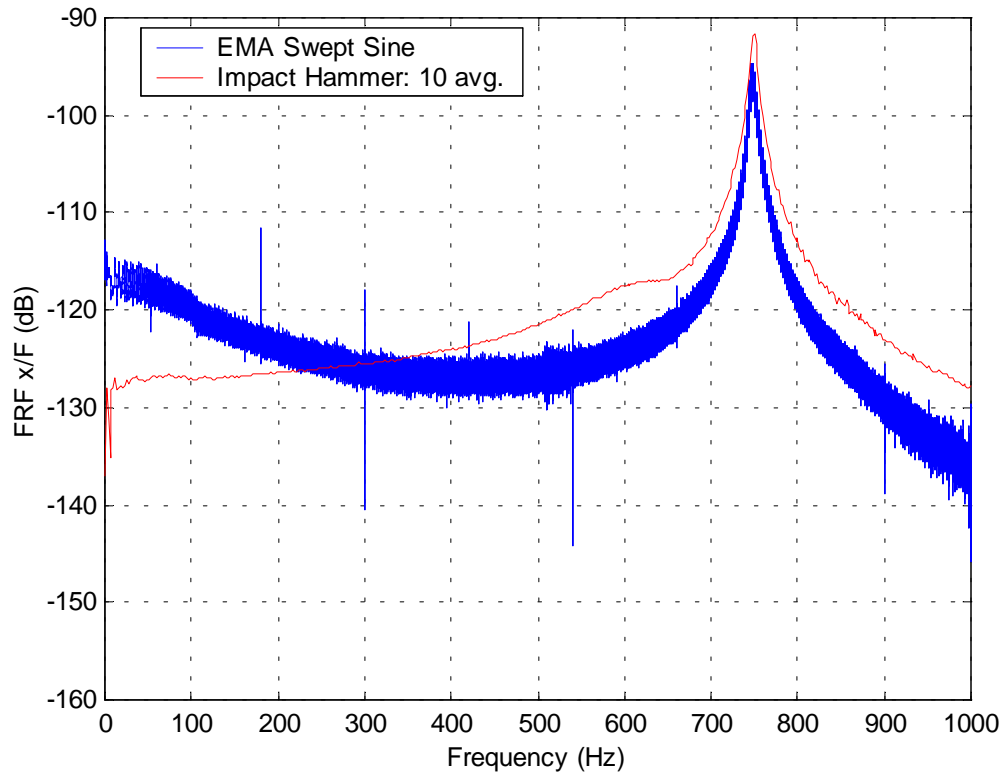


**Figure 6.4: EMA and impact hammer (10 averages) FRFs for a 4.00” overhang tool blank**

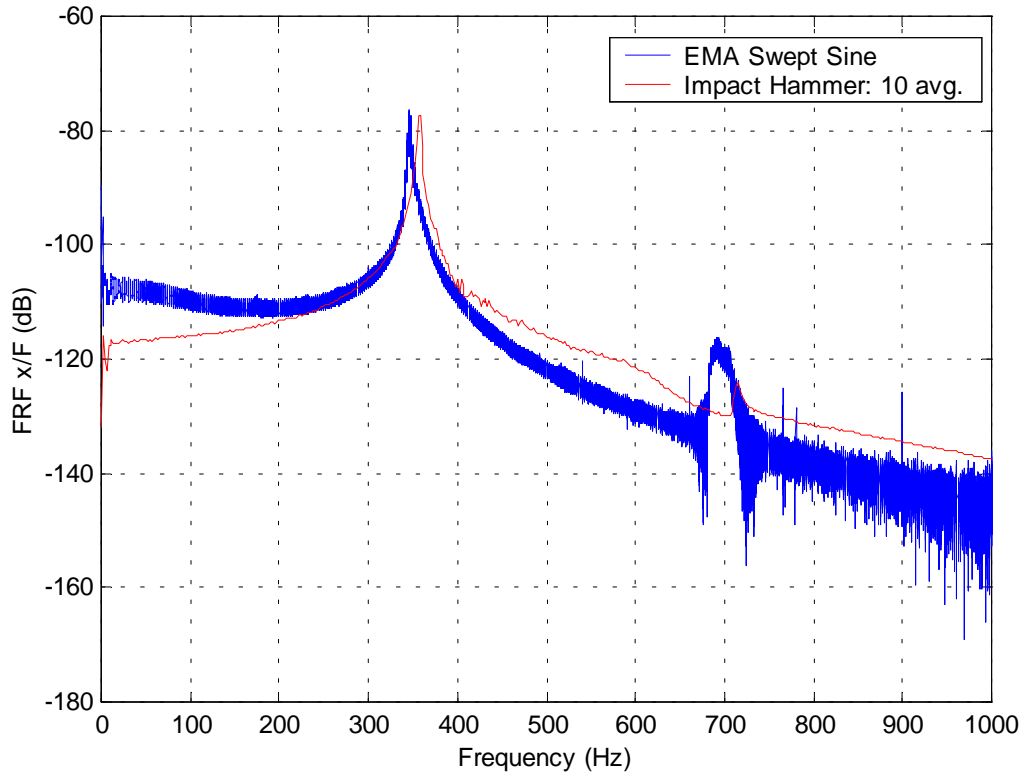


**Figure 6.5: EMA and impact hammer (10 averages) FRFs for a 6.00” overhang tool blank**

One important observation from these plots is that the DC compliances (approximately -115 dB for the 4.00” overhang tool blank in Figure 6.4) correspond favorably to static compliance measurements taken on this machine. These static measurements revealed a spindle compliance of approximately  $0.5 \cdot 10^{-6} \text{ m/N}$ , or -126 dB. Note also the appearance in Figure 6.5 of a second harmonic peak at about 700 Hz and 710 Hz in the EMA and impact hammer curves, respectively.

Figure 6.6 shows FRF test results (EMA and impact hammer) for a 3.50” overhang, 4-flute HSS end mill. For these tests, the first natural frequencies are 918 Hz and 882 Hz from the EMA and impact hammer, respectively.

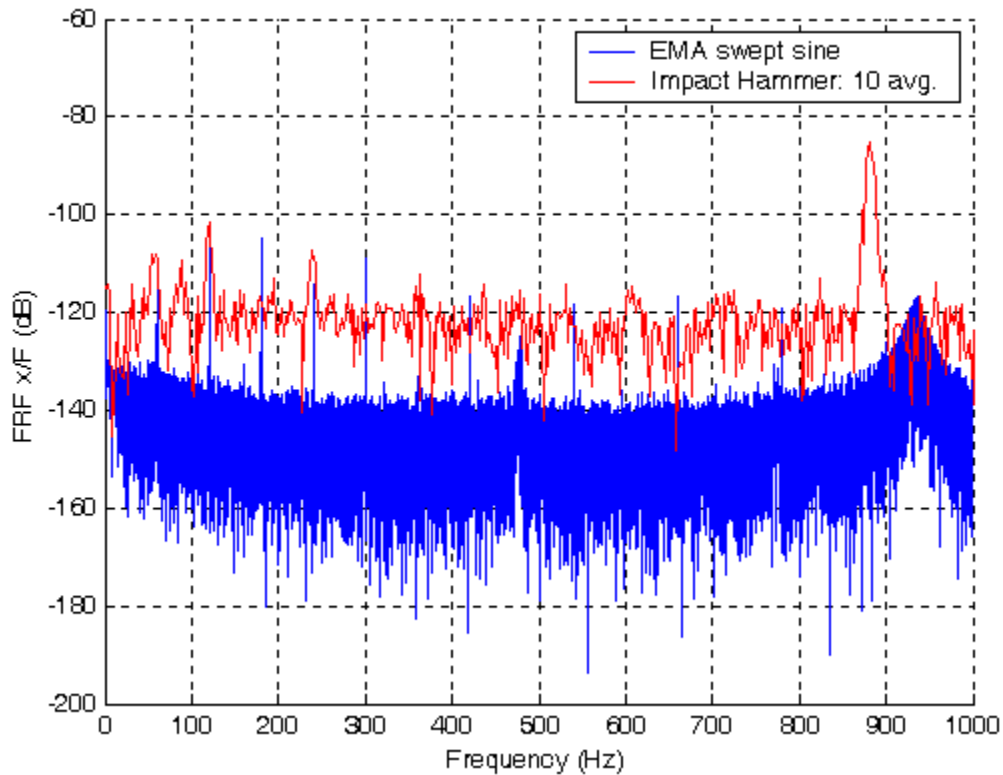


**Figure 6.6: EMA and impact hammer (10 averages) FRFs for a 3.50” overhang, 4-flute HSS end mill**

Overall, the EMA modal testing results showed good agreement with the impact hammer results. Small discrepancies between EMA and impact hammer FRFs may result from inconsistencies associated with impact hammer testing. They may indicate that the impact was not “clean;” i.e. there may have been a double hit or extended contact between the tool and the hammer tip. Variations may also result from irregular geometry of the tool (associated with flutes, etc.); the impact hammer may have hit the tool in a direction with a slightly lower stiffness.

There appear to be 60 Hz line noise peaks evident in the FRF plots of Figures 6.4, 6.5, and 6.6. Harmonics of this signal appear at multiples of 60 Hz as well. These peaks can be seen in both the impact hammer and the EMA curves. These effects can be eliminated with shielding and filtering, but these actions were not pursued.

#### 6.4.2 EMA Modal Tests: Rotating Tools

In order to test the pulse-shaping capabilities of the EMA, FRF tests were conducted on rotating, half-round tool blanks. The ability to accurately shape force profiles in real-time could potentially enable the EMA to impart forces on spinning cutting tools of arbitrary geometry, and enable true FRF measurements at cutting speeds. Changes in the FRF measurements due to dynamic damping and stiffness variations could thus be determined.

Rotating FRF tests required modifications to the standard tool blank. To simulate a cutting tool passing the EMA poles, one end of the tool blank was ground to a half-round section, as shown in Figure 6.7.



**Figure 6.7: Closeup of half-round tool blank**

The EMA was tested on the half-round tool blanks in both “synchronous” and “asynchronous” modes. Synchronous mode tests were performed by applying the excitation force to the rounded face of the tool blank and simultaneously measuring the displacement of the opposite side of the blank. Asynchronous tests involved measuring the displacement of the rounded face one-half rotation after the application of the excitation force.

The same EMA hardware and setup (Figures 3.2 and 6.3) used in the non-rotating tests was employed for the rotating tests. The excitation force was triggered by a threshold set

on the ODS displacement signal. The actuator force profile consisted of one period of a sine wave with an amplitude of 10.0 A and a swept period (Figure 6.8 a and b) less than one half of the tool rotation period. A summary of experiments conducted is presented in Table 6.2.

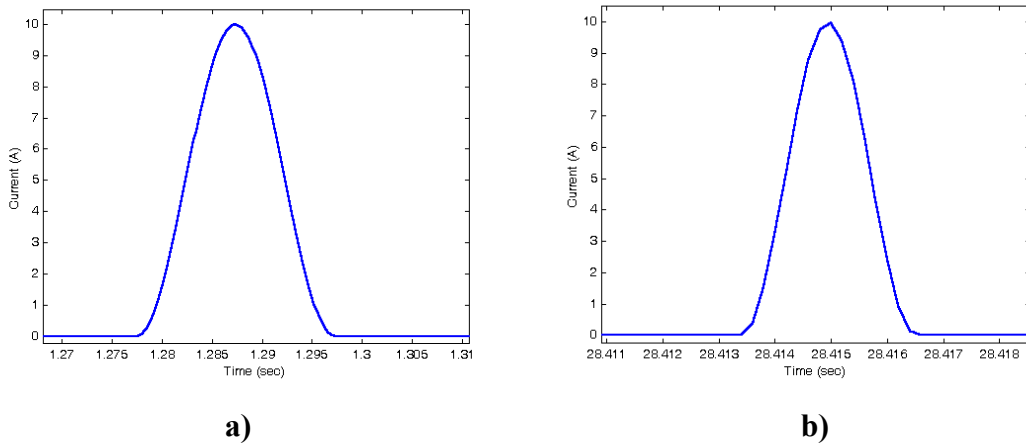


**Figure 6.8: EMA force profile used to excite rotating half-round tool blanks a) low frequency sinusoidal pulse b) higher frequency sinusoidal pulse**

**Table 6.2: EMA modal testing summary for rotating specimens**

<b>Tool</b>	<b>Overhang Length</b>	<b>Spindle Speed</b>	<b>Excitation Source</b>	<b>Excitation Profile</b>
half-round blank	1.50"	1200 rpm	EMA	full-period sine
half-round blank	3.50"	1200 rpm	EMA	full-period sine
half-round blank	4.00"	1200 rpm	EMA	full-period sine
half-round blank	6.00"	1200 rpm	EMA	full-period sine

FRF results for a 3.50" overhang, half-round tool blank rotating at 1200 rpm are shown in Figure 6.9.

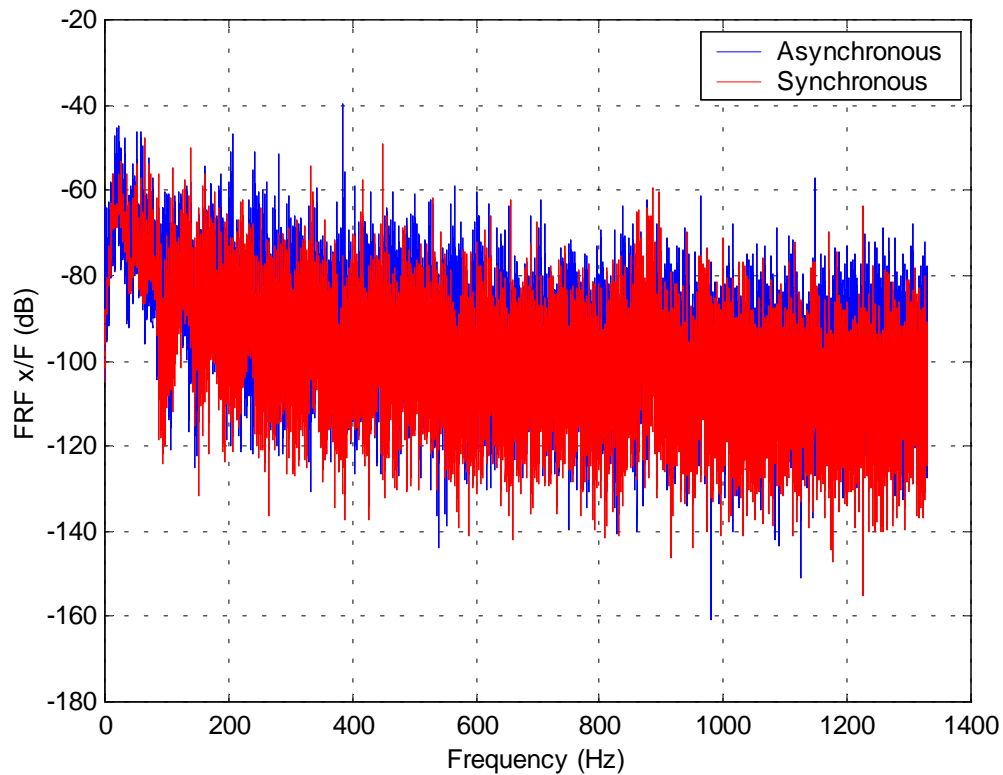


**Figure 6.9: EMA FRF of a 3.50” overhang, half-round tool blank rotating at 1200 rpm**

These unfiltered results are very noisy and do not reveal an obvious tool mode, although there appears to be a peak at about 875 Hz. The EMA and impact hammer results for a non-rotating tool predict a first natural frequency at 918 Hz and 880 Hz, respectively. Detailed inspection of Figure 6.9 reveals a synchronous mode near 20 Hz (equivalent to a spindle speed of 1200 rpm), and harmonics of this peak are a major contributor to the noise. Tool runout, which was measured to be around 20  $\mu\text{m}$ , adds this synchronous harmonic component to the tool response. This effect could be filtered out during data collection, but this approach was not pursued. With synchronous data filtering, the determination of FFTs using real-time pulse shaping could be greatly enhanced. In FRF plots for longer tools, these runout harmonics were great enough to obscure all modal peaks.

## 6.5 Stability Lobe Diagram Verification

As discussed in Section 3.4, the ultimate utility of the EMA lies in its ability to function as part of a chatter prediction and avoidance system for HSM applications. Thus, demonstrating that the FFTs computed from EMA tests accurately predict stable cutting regions is critical to demonstrating the feasibility of this approach.

To demonstrate this utility on a commercial machine, FRF data was generated for a non-rotating, 4.00" overhang, 4-flute HSS end mill chucked in the spindle of a Haas VF-1 5-axis vertical machining center. This FRF was used to produce a SLD, which was in turn verified by cutting tests performed on the Haas VF-1. Three different spindle speeds were used to verify the existence of a stable cutting region in an expected location.

From the FRF, the first natural frequency of the tool/spindle/machine system was determined to be 718 Hz. The stability limit,  $b_{lim}$ , was calculated using (2.3) [39]. As detailed in Section 2.3.2,  $b_{lim}$  is the deepest cut that can be made at all spindle speeds without chatter:

$$b_{lim} = \frac{-I}{2K_s \operatorname{Re}(FRF)_{min}} \quad (6.1)$$

where:

$K_s$  = specific force of the workpiece material (N/mm<sup>2</sup>)

$\operatorname{Re}(FRF)$  = real part of the tool/spindle/machine system FRF

A SLD was generated from the experimental FRF using analytical methods outlined in Sections 2.3 and 2.4. As defined in (2.2) [34]:

$$b = \frac{-1}{2K_s \mu \operatorname{Re}(FRF)} \quad (6.2)$$

where:

$b$  = stability lobe boundary (mm)

$\mu$  = directional orientation factor

This SLD, presented in Figure 6.10, reveals a primary stability peak at 10,770 rpm and a secondary peak at 5,385 rpm. Although the primary peak lies above the spindle speed capabilities of the Haas VF-1, this SLD predicts that there will be a region of stable cutting around 5,385 rpm. In this region, cuts can be made significantly deeper than the stability limit  $b_{lim}$ .

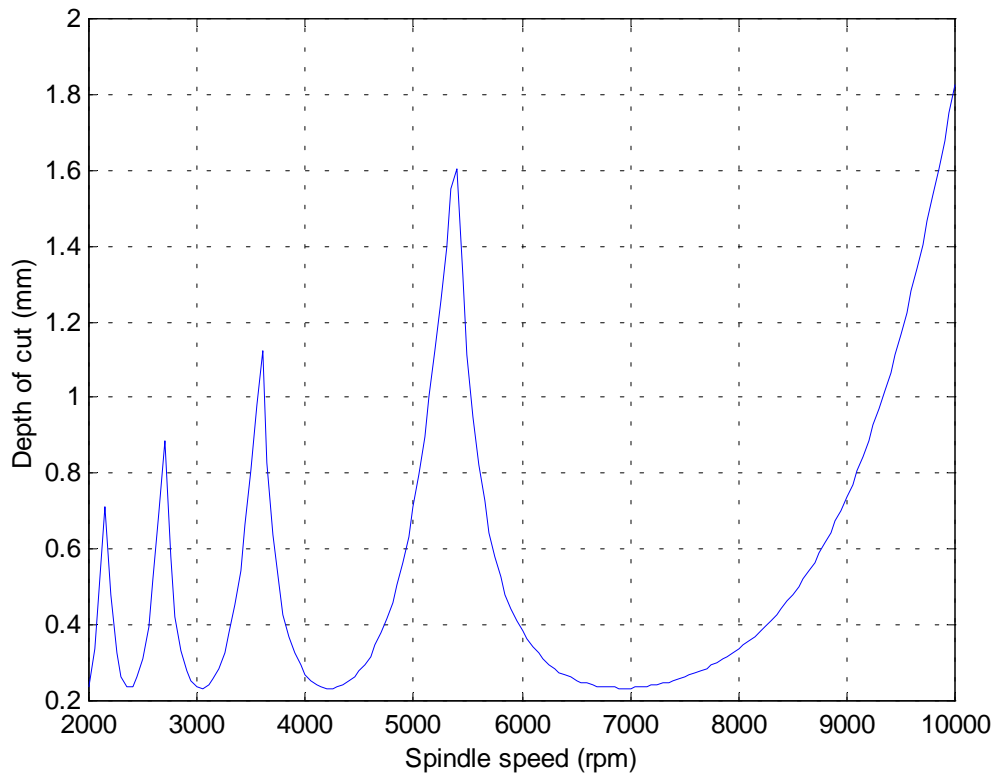


**Figure 6.10: SLD for a 4.00", 4-flute HSS end mill [28]**

To verify this prediction, cutting data was collected using an accelerometer mounted to a  $\frac{3}{4}$ " thick, 6061 T6 aluminum workpiece. The workpiece was faced to ensure accurate and consistent cutting depths. Slotting cuts were made at a variety of depths, starting at 0.1 mm and stepping to 1.5 mm in 0.2 mm increments. All depths were cut at three different spindle speeds: 4,000, 5,385, and 7,000 rpm. The cuts at 4,000 and 7,000 rpm were expected (based on the SLD) to produce chatter at low immersion, while cuts at 5,385 rpm were expected to reside in an area of cutting stability.

Chatter was evaluated using three criteria. The first criterion was audible: by 'listening' it was possible to discern changes in cutting noise volume and pattern (beating for example). The second criterion was visual: the surface finish of the workpiece was examined closely after cutting. The final, and most quantitative, involved measuring and evaluating cutting vibrations as sensed by a PCB U353B65 piezoelectric accelerometer attached to the plate. Both the raw accelerometer data (time domain) and FFT data (frequency domain) were examined. Raw data for three representative cuts at a cutting depth of 0.7 mm are presented in Figure 6.11. The FFT of this data follows in Figure 6.12.

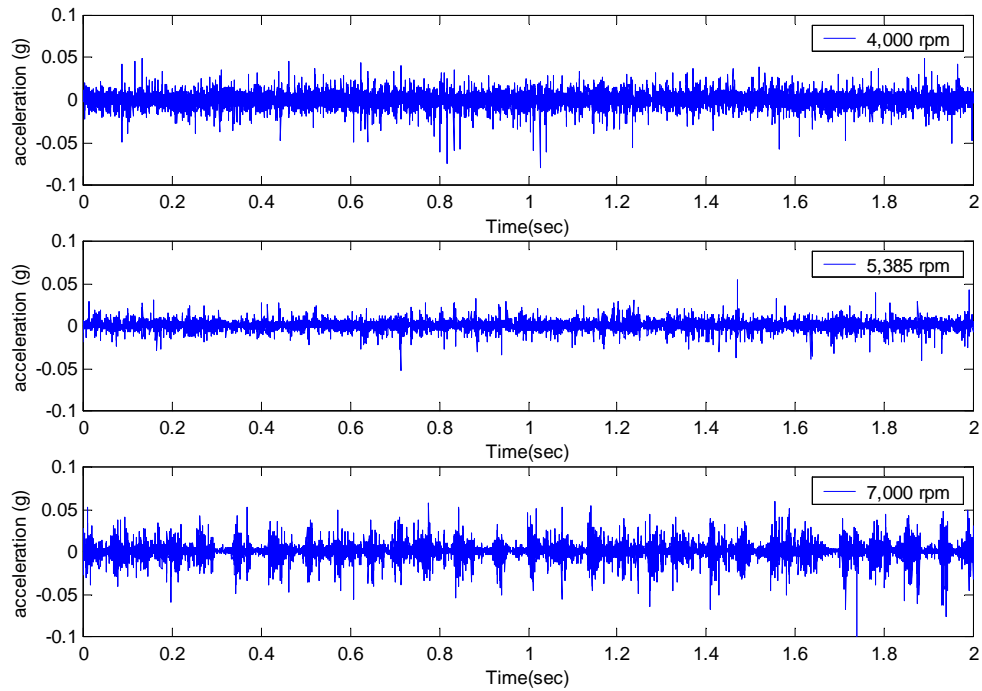


**Figure 6.11: Acceleration time responses for a 4.00” overhang, 4-flute end mill at three different spindle speeds: 0.7 mm cutting depth**

The beating phenomenon can be clearly seen in the third plot (7,000 rpm) of Figure 6.11. This beating was plainly audible as the cut was being made.

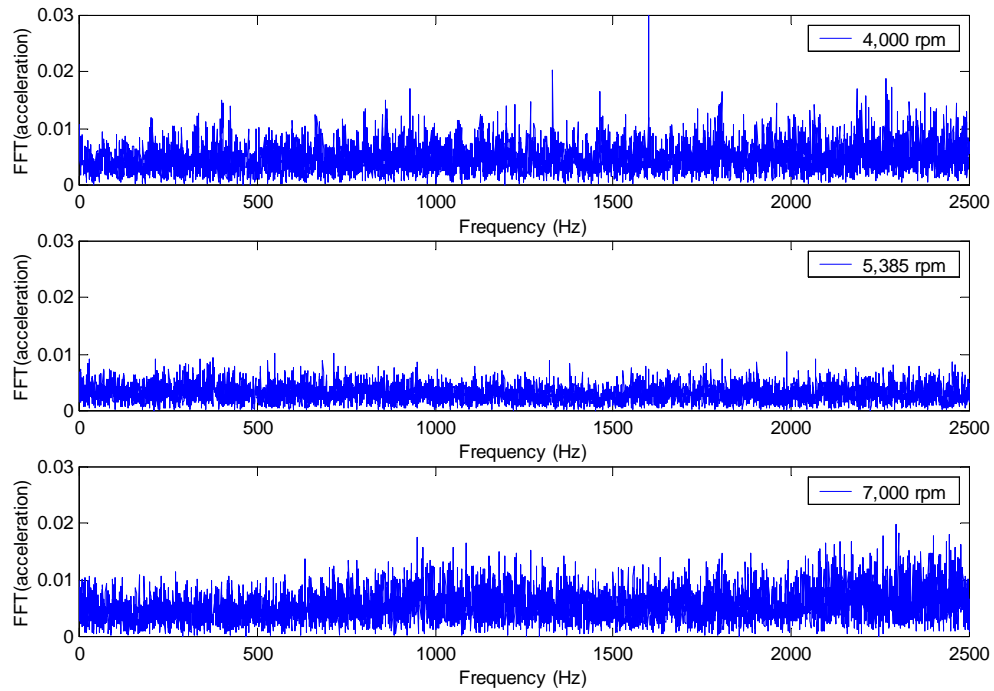


**Figure 6.12: Acceleration frequency responses for a 4.00” overhang, 4-flute end mill at three different spindle speeds: 0.7 mm cutting depth**

Inspection of Figures 6.11 and 6.12 reveals that the overall magnitude of the response is lower for the 5,385 rpm cuts than for the 4,000 rpm and 7,000 rpm cuts. This conclusion is supported by comparing RMS cutting accelerations (measured normal to the workpiece) for these three cuts, as compiled in Table 6.3.

**Table 6.3: Computed RMS accelerations for 0.7 mm deep slotting cuts**

<b>Spindle Speed</b>	<b>RMS Acceleration</b>
4,000 rpm	0.3113
5,385 rpm	0.1222
7,000 rpm	0.3889

Similar differences appeared in the data of several other cutting tests. Though chatter is very difficult to define exactly, the trend in differences between the cutting energies at

the different spindle speeds investigated is consistent with the audible and surface finish indicators monitored during and after the cutting. The resulting experimental cutting data points are superimposed on the predicted secondary stability peak near 5,400 rpm in Figure 6.13. Cuts where chatter was unquestionably encountered are marked on the plot with an “X” and cut points where there was a less intense response are indicated with a “O”.

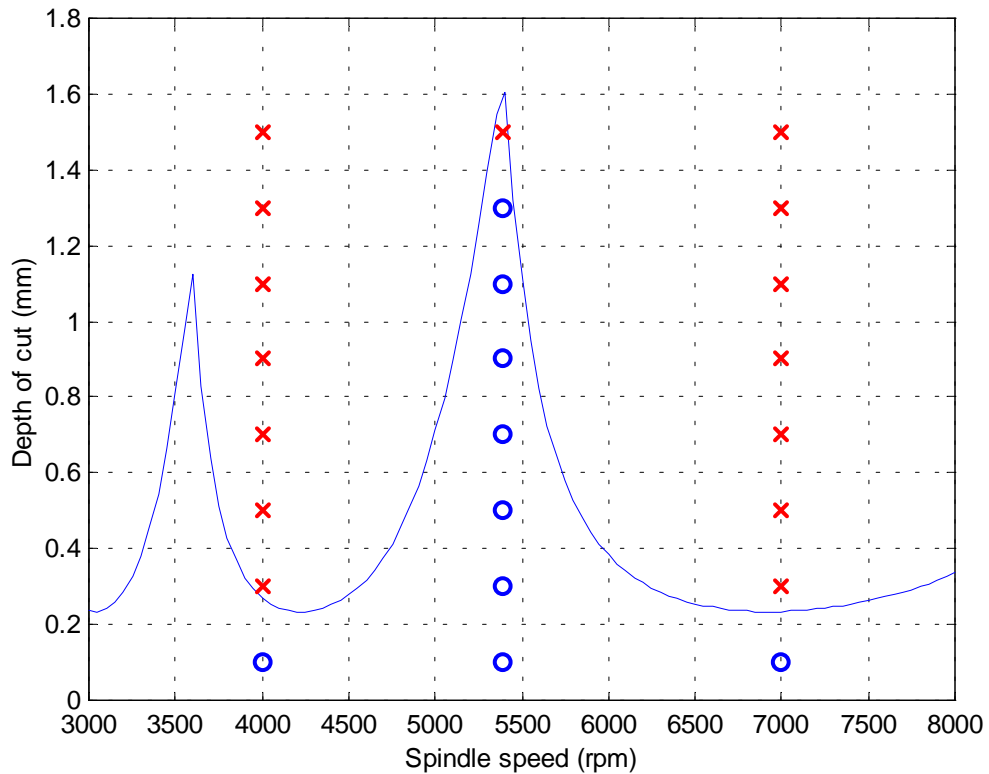


**Figure 6.13: Cutting test results for 4.00” overhang, 4-flute end mill [28]**

The SLD (Figure 6.10 and 6.13) generated using the EMA accurately predicts regions of stability for this tool and machine. This verifies the analytical approach to chatter and stability prediction. It also indicates that the EMA, given its advantages over other testing methods discussed in Chapter 3, can be a valuable tool in chatter avoidance, and a key component in a predictive, chatter avoidance system.

## **6.6 Summary of Test Results**

The experimental test results presented in this chapter clearly demonstrate the feasibility of the EMA device as part of a chatter prediction and avoidance system for HSM applications. Tests verified the force and flux predictions derived using analytical methods (MCA, GMT, and FEA) for a variety of tool materials, tool sizes, input current amplitudes and waveforms. Additional tests confirmed that FRFs produced using the EMA produce comparable, and perhaps superior, results to those obtained using a traditional vibration testing method - impact hammer testing. FRF tests conducted on stationary (non-rotating) and rotating tools and blanks of various materials and dimensions revealed the expected modal characteristics and demonstrated the capabilities of the EMA. Most importantly, cutting tests on a commercial CNC milling machine demonstrated the ultimate utility of the EMA device as part of an automated chatter prediction system. These cutting tests substantiate regions of chatter and stable cutting predicted using EMA data.

## 7 Conclusions and Future Work

### 7.1 Conclusions

This thesis detailed the design, development and operational verification of a non-contacting electromechanical actuator that can be used as part of an automated chatter prediction and avoidance system for high-speed machining (HSM) operations. In machining operations where very tight tolerances are required or surface quality is critical, in-situ chatter detection and control methods are unacceptable: these techniques cannot prevent chatter, they can only attempt to eliminate or reduce its adverse effects. For these critical machining operations, chatter prediction and avoidance methods are necessary. Accurate chatter prediction requires knowledge of the machine's dynamic characteristics, chiefly the first natural frequency of the tool/spindle/machine system. Although chatter prediction methods based on standard modal testing methods are accurate, these test procedures are difficult to perform in machine shop environments and can require expensive equipment.

A non-contacting, permanent magnet device developed at NIST introduced a new approach to the modal testing phase of chatter prediction. This device relies on a permanent magnet to passively excite the dynamics of a rotating machine tool. The electromagnetic actuator (EMA) developed as part of this research extends the capabilities of the NIST device to provide controllable, non-contacting excitation for modal tests on machine tools. This EMA device offers the advantages of being accurate, easy to use, and applicable to a wide variety of tools and operating conditions. These advantages are related to its capabilities: high force amplitude, high bandwidth, and controllable force profiles.

The EMA system was designed with enough force amplitude (6.75 N) and bandwidth (1000 Hz) to adequately excite a representative range of tool materials (HSS, carbide, etc.), tool geometries (fluted end mills, tool blanks, etc.), and tool dimensions.

Analytical methods used in the design process enabled the performance of different designs to be evaluated before hardware was produced. Experimental device testing on stationary and rotating tools validated these analytical results, indicating that simulation-based design may be used to accurately predict the performance of future versions of this actuation system.

Extensive testing was conducted to demonstrate the ultimate utility of this device in an automated chatter prediction and avoidance system for HSM applications. Tests were conducted on a range of cutting tools and tool blanks to assess the reliability of FRF results produced by the EMA. The device provided frequency response results that were accurate, repeatable, and in some respects superior to impact hammer results. Experiments were also performed to demonstrate the actuator's pulse-shaping capabilities on rotating tool blanks. Finally, tests were conducted to validate regions of chatter and stable cutting predicted using EMA data. Results indicate that stability lobe diagrams (SLDs) generated using the EMA accurately predict preferable operating conditions for avoiding chatter.

## **7.2 Future Work**

Although the EMA device demonstrated acceptable performance for a range of operating conditions, certain modifications might result in a more feasible product for commercial HSM applications.

### **7.2.1 Real-time Data Filtering**

As noted in Section 6.4.2, harmonics of the tool's rotational frequency appeared to overwhelm frequency response data in rotating tool tests. Synchronous data filtering would produce cleaner FRFs for rotating blanks and cutting tools. This would be especially useful for specimens longer than 4.00", as excessive runout prevented identification of their modal characteristics. 60 Hz line noise could also be filtered out

during data collection to avoid its appearance in the FRF results. These filtering operations would enhance the accuracy and extend the capabilities of the EMA system.

### 7.2.2 Self-Sensing Capabilities

The EMA system utilized a high-performance optical displacement sensor to measure tool deflections with a resolution of  $0.25\ \mu\text{m}$ . Unfortunately, these sensors are relatively expensive and their accuracy is influenced by optical properties of the tool. It may be possible to eliminate separate displacement sensing by incorporating this capability into the design of the EMA. This capability could take the form of an additional coil wound around the actuator core. The change in the air gap caused by the deflection of the tool would change the flux linkage between the tool and the actuator core. This change would produce a measurable voltage that varies with the gap width, potentially enabling accurate displacement measurements.

## References

- [1] Altıntaş, Y., Budak, E., 1995, "Analytical Prediction of Stability Lobes in Milling," *Annals of the CIRP* Vol. 44/1/95: 357-362.
- [2] Bala-Dyne: US Patent #5,757,662, [www.baladyne.com](http://www.baladyne.com).
- [3] Ber, A., Rotberg, J., Zombach, S., 1988, "A Method for Cutting Force Evaluation of End Mills," *Annals of the CIRP* Vol. 37/1/88: 37-40.
- [4] Bishop, R. E. D., Johnson, D. C., 1960, "The Mechanics of Vibration," Cambridge University Press, Cambridge, England.
- [5] Davies, Matthew A., Pratt, Jon R., Dutterer, Brian, 2002, "Device for Stable Speed Determination in Machining," U. S. Patent #6,349,600.
- [6] Delio, T., Tlusty, J., Smith, S., 1992, "Use of Audio Signals for Chatter Detection and Control," *Transactions of the ASME Journal of Engineering for Industry*, Vol. 114, pp. 146-157.
- [7] Delio, T. S., 2000, NCMS presentation on "Spindle Dynamics," conference proceedings: <http://techcon.ncms.org/00fall/> "Spindle Dynamics (modeling and prediction)"
- [8] Drozda, Thomas J., Wick, Charles, Ed., 1983, "Tool and Manufacturing Engineers Handbook, Vol. 1," SME, Dearborn, MI.
- [9] E.E.Staff, M.I.T., 1965, "Magnet Circuits and Transformers," M.I.T. Press, Cambridge, MA.
- [10] Ewins, D. J., 1984, "Modal Testing: Theory and Practice," John Wiley & Sons Inc., New York.
- [11] Fitzgerald, A. E., Higginbotham, D. E., Gabel, A., 1981, "Basic Electrical Engineering," 5<sup>th</sup> Ed., McGraw-Hill, New York.
- [12] Fitzgerald, A. E., Kingsley, Charles Jr., Umans, Stephen D., 1990, "Electric Machinery," McGraw-Hill Inc., New York.
- [13] Gere, James M., Timoshenko, Stephen P., 1997, "Mechanics of Materials," PWS Publishing Co., New York.
- [14] <http://femm.berlios.de/> FEMM<sup>®</sup>.

- [15] <http://www.kennametal.com/metalworking/html/milling/BestSPEED.htm>  
Kennametal BestSPEED™ analyzer.
- [16] <http://www.mech.ubc.ca/~mal/research/maltf/measure.html> MalTF.
- [17] <http://www.mfg-labs.com/Harmonizer/> Ingersoll Rand, Harmonizer.
- [18] [http://www.woojooitech.com/product/pdf/PI/Capacitive%20Sensor\(250%20k\).pdf](http://www.woojooitech.com/product/pdf/PI/Capacitive%20Sensor(250%20k).pdf).
- [19] Landers, Robert G., Ulsoy, A. Galip, Furness, Richard J., 1999, "Process Monitoring and Control of Machining Operations", *Analysis of Mechanical Systems*, CRC Press (submitted).
- [20] Li, T. C., Tarn, Y. S., Chen, M. C., "A Self-Organising Neural Network for Chatter Identification in Milling," 1996, *International Journal of Computer Applications in Technology*, Vol.9, No.5-6: 239-48.
- [21] Maia, Nuno M. M., Silva, Julio, M. M., 1997, "Theoretical and Experimental Modal Analysis," John Wiley & Sons Inc., New York.
- [22] Merritt, H. E., 1965, "Theory of Self-Excited Machine Tool Chatter," *ASME J. for Eng. in Industry*, 87, 447-454.
- [23] Minis, I., Yanushevsky, T., Tembo, R., and Hocken, R., 1990, "Analysis of Linear and Nonlinear Chatter in Milling," *Annals of the CIRP*, 39: 459-462.
- [24] Modern Machine Shop 8/99 online supplement:  
[www.mmsonline.com/articles/089903.html](http://www.mmsonline.com/articles/089903.html)
- [25] Modern Machine Shop 8/01 online supplement:  
<http://www.mmsonline.com/hsm/0801.html>
- [26] Naterwalla, Urmaze, 2000, "Chatter-Free Milling And Optimized Material Removal Rates: Analysis Of Chatter In Milling," *Modern Machine Shop*, March 2000 Online Supplement.
- [27] Patrick, G. B., 1983, "Practicalities of Acquiring Valid Data During Modal Tests," *Procedures of the 3<sup>rd</sup> International Modal Analysis Conference (IMAC III)*, Orlando, FL, pp. 845-849.
- [28] Ren, Yongfu, 2001, personal communication, November 11.
- [29] Schmitz, T., Donaldson, R., 2000, "Predicting High-Speed Machining Dynamics by Substructure Analysis," *Annals of the CIRP*, Vol. 49/1: 303-308.

- [30] Schmitz, T. L., Davies, M. A., Medicus, K., Snyder, J., 2001, "Improving High-Speed Machining Material Removal Rates by Rapid Dynamic Analysis," *Annals of the CIRP*, Vol. 50/1: 263-268.
- [31] Shiraishi, M., Kume, E., 1988, "Suppression of Machine-Tool Chatter by State Feedback Control," *Annals of the CIRP* Vol. 37/1: 369-372.
- [32] Slemon, Gordon, 1966, "Magnetolectric Devices Transducers, Transformers, and Machines," New York, John Wiley and Sons, Inc.
- [33] Smith, S., Tlusty, J., 1990, "Update on High Speed Milling Dynamics," *Trans. ASME, Journal of Engineering Industry*, 112: 142-149.
- [34] Smith, S., Tlusty, J., 1992, "Stabilizing Chatter by Automatic Spindle Speed Regulation," *Annals of the CIRP* Vol. 41/1: 433-436.
- [35] Smith, S., "Explosive Excitation Method and Device," Application for U.S. Patent, submitted April 2000.
- [36] Sridhar, R., Hohn, R. E., and Long, G. W., 1968, "A Stability Algorithm for the General Milling Process," *Trans. ASME Journal of Engineering for Industry*, Vol. 90: 330-334.
- [37] Thomson, William T., Dahleh, Marie Dillon, 1998, "Theory of Vibrations with Applications," 5<sup>th</sup> Ed., Prentice Hall, New Jersey.
- [38] Tlusty, J., Polacek, M., 1963, "The Stability of The Machine Tool Against Self Excited Vibration," *Prod. Eng. Res. Conf.*, ASME, Pittsburgh.
- [39] Tlusty, Jiri, 2000, "Manufacturing Processes and Equipment," Prentice Hall, Upper Saddle River, NJ.
- [40] Tobias, S. A., "Machine Tool Vibrations," London: Blackie & Son.
- [41] Unigraphics NURBS white paper, [http://www.plmsolutions-eds.com/publications/whitepapers/HSM\\_whitepaper.pdf](http://www.plmsolutions-eds.com/publications/whitepapers/HSM_whitepaper.pdf).
- [42] Zelinski, P.C., 1998, "Scanning the Horizon: Chatter Control In A Box," "Modern Machine Shop" magazine July, 1998, <http://www.mmsonline.com/articles/0798scan2.html>